International Journal of Steel Structures (2018) 18:650–673
https://doi.org/10.1007/s13296-018-0025-y

Experimental Investigation of Aluminum Alloy and Steel Core Buckling Restrained Braces (BRBs)

Cigdem Avci-Karatas[1] · Oguz C. Celik[2] · Cem Yalcin[3]

Received: 26 April 2017 / Accepted: 21 December 2017 / Published online: 3 May 2018

Abstract
Buckling restrained braces (BRBs) display balanced hysteretic behavior under reversed cyclic tension and compression forces and dissipate a significant amount of seismic energy during credible earthquakes. This paper reports on an experimental investigation of newly developed BRBs with different core materials (steel and aluminum alloy) and end connection details. A total of four full-scale BRBs with two steel cores and outer tubes (BRB-SC4 and BRB-SC5) as well as two with aluminum alloy cores and aluminum outer tubes (BRB-AC1 and BRB-AC3) with specific end details were designed as per the AISC Seismic Provisions, manufactured and cyclically tested. These tests made it possible to compare the impact of the steel and aluminum alloy material characteristics on the hysteretic behavior and energy dissipation capacities. The proposed steel and aluminum alloy core BRBs with various end details achieved the desired behavior, while no global buckling occurred under large inelastic displacement cycles.

Keywords Steel, aluminum alloy · Buckling restrained brace (BRB) · Hysteretic behavior · Experimental study

1 Introduction

Theoretical and experimental research is underway to develop new cost-effective buckling restrained brace (BRB) technologies. Since steel moment-resisting frames did not demonstrate the expected performance during the 1994 Northridge and 1995 Kobe earthquakes, new solutions that could minimize the destructive effects of earthquakes have been sought. Metallic dampers (e.g., the shear panel system (SPS), eccentrically braced frame (EBF), triangular added damping system (TADAS), and vertical shear link (VSL) devices) of various types that dissipate seismic energy have beneficial results in this sense (e.g., Christopoulos and Filiatrault 2006). BRBs (also known as unbonded braces), on the other hand, are metallic dampers, and they display balanced hysteretic behavior through axial yielding under reversed cyclic tension and compression forces. Symmetrical and robust behavior of BRBs under both tension and compression without any significant strength and stiffness degradation results in stable hysteretic behavior with maximum energy dissipation. Furthermore, when compared to other alternative seismic energy dissipation systems, BRBs have several advantages, such as ease of manufacture with simple end connection details as well as ease of construction and replacement after a strong earthquake. BRBs can also be used in existing structures for seismic retrofit purposes to achieve the required strength, stiffness, and ductility mandated by the new codes. A numerical comparative study has been performed to assess seismic responses of a 9-story steel existing moment frame building retrofitted with different bracing systems including BRBs (Di Sarno and Elnashai 2009).

Experimental and numerical studies have been conducted by several researchers to show the effectiveness of different types of BRBs. Sabelli et al. (2003) analytically investigated the seismic response of frames with BRBs (i.e., BRBFs) that

✉ Cigdem Avci-Karatas
cigdem.karatas@yalova.edu.tr

Oguz C. Celik
celikoguz@itu.edu.tr

Cem Yalcin
yalcince@boun.edu.tr

[1] Department of Transportation Engineering, Faculty of Engineering, Yalova University, Yalova 77100, Turkey

[2] Structural and Earthquake Engineering Division, Faculty of Architecture, Istanbul Technical University, Taskisla, Taksim, Istanbul 34437, Turkey

[3] Department of Civil Engineering, Bogazici University, Bebek, Istanbul 34342, Turkey

included a number of parameters, such as ground motion characteristics and various structural configurations. Fahnestock et al. (2003) addressed the global ductility demands of BRBFs and local ductility demands of BRBs using nonlinear time history analyses, and the results were compared to the BRBF Recommended Provisions given in AISC (2001) and SEAOC (2001). Takeuchi et al. (2008, 2014) proposed a simple method for predicting the cumulative deformation and energy dissipation capacities of BRBs under random amplitudes. Takeuchi et al. (2012) also reported on the local buckling condition of the core plate as well as the design criteria to prevent local failure of the casing. A simplified method based on an equivalent linearization to design the required amount of BRB and elastic steel frame (SF) capacity for retrofitting purposes of existing reinforced concrete (RC) school buildings was proposed by Sutcu et al. (2014). Experimental studies on non-ductile RC frames with and without BRBs have been conducted by Di Sarno and Manfredi (2010, 2012). Several advantages of using BRBs as the seismic retrofit option are discussed. Usami et al. (2008) studied the buckling prevention condition with a series of well-controlled experiments. Vargas and Bruneau (2009a, b) proposed an alternative design for systems with metallic fuses composed of BRBs. An experimental study was also conducted on a three-story frame designed with BRBs to verify the proposed design procedure. A series of performance tests and analyses were carried out by Usami et al. (2009) to clarify the requirements of high-performance BRBs for the damage-controlled seismic design of steel bridges. Celik and Bruneau (2009, 2011) analytically investigated the optimum geometrical layout to maximize the dissipated hysteretic energy in ductile end diaphragms with BRBs in straight and skewed slab-on-girder steel bridges. Component tests were conducted by Zhao et al. (2012) to address the effect of brace end rotation on the global buckling behavior of pin-connected BRBs with end collars. To increase the efficiency of BRBFs, a novel connection with a gusset plate connected to only the beam and offset from the column face was proposed and tested in a three-story building frame under quasi-static loading by Berman and Bruneau (2009). The experimental hysteretic behavior of BRBs with bolted and welded end connections was investigated for comparison purposes by Fujishita et al. (2015). Near full-scale displacement-controlled reversed cyclic tests were performed, and the specimens showed stable cyclic performance until reaching 3% axial strain. However, the welded end connection led to a slightly lower cyclic performance because it fractured earlier compared to the bolted connection. Sahoo et al. (2015) proposed a passive energy dissipation device called as shear-and-flexure yielding damping (SAFYD) and investigated load-carrying capacity, hysteretic response, energy dissipation, equivalent viscous damping, and ductility to match the test results with a predicted finite element (FE) analysis. A series of cyclic tests was carried out by Chou et al. (2015) to conduct experimental studies that established a direct comparison basis between dual-core self-centering braces (DC-SCBs) and sandwiched buckling-restrained braces (SBRBs) designed with similar axial capacity and length. Tests have shown that the DC-SCB and SBRB exhibit robust cyclic performances with good deformation capacity and durability. An analytical study by Pandikkadavath and Sahoo (2016) concluded that the optimum reduction in yielding core lengths of BRBs could improve the overall seismic response of BRBFs with a reduction in the residual drift response.

Aluminum is increasingly being used in a variety of structural engineering applications due to its superior characteristics, such as lightweight, high strength-to-weight ratio, good corrosion resistance, durability, recyclability properties, high strength similar to steel and excellent formability (e.g., extrusion). These characteristics are of particular significance to the design of lightweight and transportable BRBs, for which the ease and speed of construction, low maintenance, and long service life are important considerations. These considerations motivated the research presented in this paper to study and develop special aluminum alloy core BRBs. An aluminum alloy core BRB is a relatively recent development in the field of BRB technology. Limited studies are available on aluminum alloy BRB experiments. In addition, no guidance exists to compare the hysteretic behavior of steel and aluminum alloy core BRBs. A series of low-cycle fatigue tests was conducted by Usami et al. (2012) to address the performance of all-aluminum alloy (without mortar) BRBs. The aluminum alloy core is separated by the restraining members by a small gap. Several experiments on welded and bolt-assembled aluminum alloy BRBs were also performed. Extruded aluminum alloy BRBs were produced and tested to address their low-cycle fatigue performance and to evaluate the effect of stoppers that were used to prevent the slip-off movement of the restraining members (Wang et al. 2013).

In this study, a total of four types of full-scale BRBs with two steel cores and two aluminum alloy cores were designed, manufactured, and tested. In particular, BRBs with aluminum alloy cores and mortar-filled aluminum alloy outer tubes were developed for the first time as an alternative to existing BRB types. Weld-free and bolted connections were used to observe the impact of the end connection detail on behavior. Quasi-static reversed cyclic loading tests were carried out in the Structural and Earthquake Engineering Laboratory (STEEL) at Istanbul Technical University.

While both BRB types with steel and aluminum alloy cores have merit in seismic applications, no guidance exists to help the engineer determine which of the two devices is preferable in terms of providing stiffness, maximum displacement ductility, and cumulative energy dissipation

capacities for a given strength. In an attempt to provide quantitative data for this purpose, this paper describes and compares the results from cyclic tests of four newly developed BRBs.

2 Materials

For the cores, two types of steel grades—locally available S235JR (ASTM A283C, normal yield strength steel) for BRB-SC4 and S355JR (ASTM A441, high yield strength steel) for BRB-SC5—and two types of aluminum alloys—commercially available A5083-H111 (nonheat-treated) aluminum alloy flat plate materials—were considered. The outer tube of steel BRBs (referred to as RT-S) was made of square hollow structural steel tubes of S355JR, whereas for aluminum alloy BRBs (referred to as RT-A), a commercially available A6060-T66 type of aluminum material with a custom extruded shape was chosen. No coupon tests were conducted on the aluminum alloy outer tubes made of A6060-T66 since these tubes were designed elastically. Instead, catalogue values obtained from the producer of the outer tube are given in Table 1. In addition, an A5083-H111 aluminum alloy material (A5083-H111, produced by adding magnesium, corrosion-resistant features and high welding strength alloy) was chosen for the core of aluminum alloy BRBs since this material has the closest yield strength to the normal yield strength steel core BRB (i.e., BRB-SC4), as shown in Fig. 1. This strength, coupled with its lightweight quality (about one-third that of steel), makes aluminum particularly advantageous, as further discussed in (Kissell and Ferry 2002). Note that the aluminum coupons were not annealed under high-temperature condition. BRBs with different core materials have been used in order to see their behavioral differences. BRB capacities were kept the same for all BRBs here for a better comparison. The core section dimensions are smaller when higher strength steel is used (Table 3). BRBs with higher strength core members could be preferred when such material is more accessible and cost effective. Since the BRBs with normal and high strength core materials, the dimensions of the non-dissipative members (beams, columns, etc.) will not be affected by using different strength steel cores.

Stress–strain relations from four tensile coupon test specimens (Fig. 1) used in the production of steel and aluminum alloy core BRBs were prepared according to the recommended ASTM standards (2008, 2009). These curves are obtained from one of the two coupon tests since both values

Table 1 Material properties of aluminum alloy cores and outer tubes

Specimen	Material grade	$\varepsilon_y^{0.2}$ (%)	ε_0 (%)	ε_u (%)	$F_{yc}^{0.2}$ (MPa)	F_{yc}^{0} (MPa)	F_u (MPa)	$\frac{F_u}{F_{yc}^{0.2}}$	E (GPa)
BRB-AC1 (core plate)	A5083-H111	0.29	0.23	17.51	182	145.60	314	1.73	73
BRB-AC3 (core plate)	A5083-H111	0.27	0.22	20.00	177	141.60	318	1.80	73
RT-A (outer tube)	A6060-T66	NA	NA	10	NA	200	227	NA	75

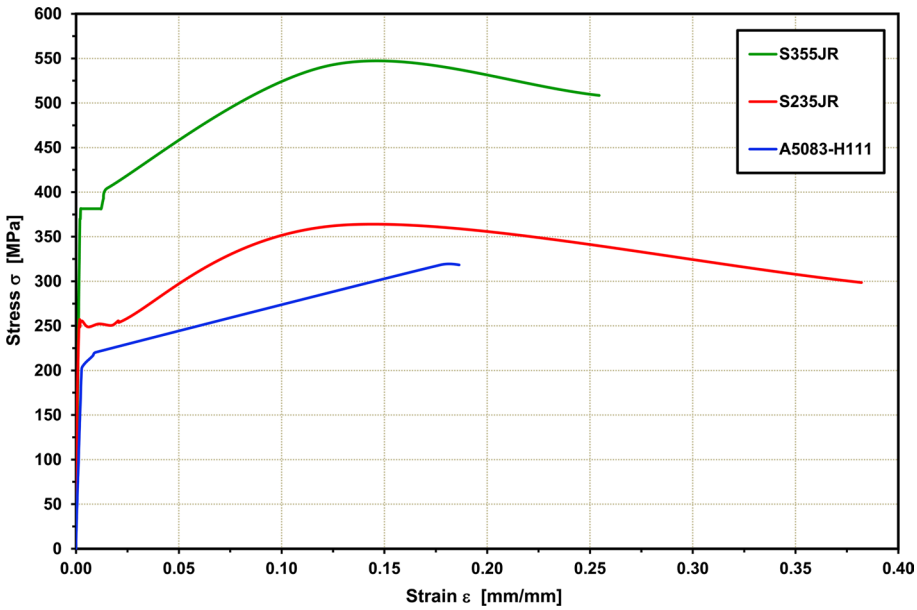

Fig. 1 Stress-strain curves from the coupon tests

were so close to each other. Post-yield strain gauges were used to determine the exact values of the yielding points, the ultimate strength, and strain as well as the modulus of elasticity of the material. Prior to testing, these material data were used in the static pushover analyses of the specimens using SAP2000 v14 (2009) to predict the load–displacement curves. The axial plastic hinge properties proposed by FEMA 356 (2000) were implemented.

The coupon test results of the aluminum alloy and steel core specimens are listed in Tables 1 and 2, respectively. These values are also obtained from one of the two coupon tests. Here, $\varepsilon_y, \varepsilon_u, F_{yc}, F_u, E$ are defined as the yield strain, total tensile strain at fracture, yield strength/stress, ultimate tensile strength/stress, and modulus of elasticity (or Young's modulus), respectively. The yield strength of the aluminum alloy BRB core coupons was calculated using the 0.2% yield strain ($\varepsilon_y^{0.2}$) offset since aluminum alloy had no definite yield plateau. $F_{yc}^{0.2}$ is the 0.2% yield strength/stress, while ε_0 is the strain, which equals $0.8\varepsilon_y^{0.2}$ for A5083-H111 (Usami et al., 2012). F_{yc}^{0} is introduced as the strength/stress corresponding to the strain ε_0. Compression tests of the high strength non-shrink mortar material revealed that the specified 7-day and 28-day mortar strengths were 52.3 and 64.1 MPa, respectively. The elastic modulus of the mortar was determined to be 37.0 GPa. The BRB specimens were tested 10 days after the mortar was placed.

The steel bolts used in the test set-up are made from A490 grade (10.9) steel. Slip-critical connections with 12M24 bolts for each end were designed per the AISC 360-10 (2010). The connection between the test set-up and gusset plates and the nominal diameter of the metric bolts was 24 mm (M24), and 12M24 bolts were used for each end. A 40 mm (M40) diameter bolted end connection (with ultimate tensile strength of 1040 MPa) was used on both ends of BRB-SC4, BRB-SC5, and BRB-AC1. On the other hand, BRB-AC3 used 16 mm (M16) diameter multi-bolted end connections.

When steel bolts are used for connections, the galvanic corrosion of steel bolts is a critical concern in aluminum alloy BRBs. Different materials, such as steel and aluminum alloy have different electrical potential, and in the presence of an electrolyte, such as a wet industrial atmosphere, the electric current flows from one material to another. This current tends to corrode the anode (aluminum alloy) and protect the cathode (steel bolts). Galvanic corrosion can be prevented by using coatings with about the same electrical potential as the base material. During the production of aluminum alloy BRBs, the bolt holes of the aluminum alloy end connection plate are protected with a thin layer of epoxy paint to prevent corrosion in this area. Dry film thickness of 15 μm was used to coat the area around the aluminum plate holes.

3 Geometric Properties of BRBs and Specimen Design

Three aluminum alloy BRB specimens (BRB-AC1, BRB-AC2, and BRB-AC3) and five steel BRB specimens (BRB-SC1, BRB-SC2, BRB-SC3, BRB-SC4, and BRB-SC5) were originally designed and manufactured (Avci-Karatas 2013). However, BRB-AC2, BRB-SC1, BRB-SC2 (slightly different from BRB-SC1) and BRB-SC3 showed poor performance during the preliminary testing mainly due to the end connection and unbonded surface details. Therefore, this study focuses on the experimental results obtained from testing BRB-AC1, BRB-AC3, BRB-SC4 and BRB-SC5. Displacement-controlled reversed cyclic tests were conducted to compare the hysteretic performances of steel and aluminum alloy BRBs. The general views, plans, and cross-sections of the specimens are shown in Fig. 2a–c for bolted end connection BRBs (BRB-AC1, BRB-SC4, BRB-SC5) and Fig. 3a–c for weld-free end connection BRB (BRB-AC3). BRBs were designed to be less than the maximum actuator capacity of 250 kN. An evaluation of the BRB specimens designed with the same base shear strength would be interesting since no guidance exists to help engineers determine which of the two devices (i.e., steel core or aluminum alloy core) is preferable in terms of providing stiffness, maximum displacement ductility, and cumulative hysteretic energy dissipation capacities for a given strength. Additionally, since both BRB types can be considered as having similar (or equal) structural behavior factors (R), an equal strength approach would be useful from the perspective of seismic design. For this reason, the BRBs were designed to achieve the same yield strength for a better comparison of their cyclic performances. The geometrical parameters are summarized in Table 3. The length and width of the yielding portions of the braces are denoted by L_{yc} and b_{yc}, respectively. Likewise, L_{con} and b_{con} are the length and width of the connection portions. The transition zone has a length of L_{tr} and a width of b_{tr}. Here, t denotes the core thickness.

Table 2 Material properties of steel cores and outer tubes

Specimen	Material grade	ε_y (%)	ε_u (%)	F_{yc} (MPa)	F_u (MPa)	$\frac{F_u}{F_{yc}}$	E (GPa)
BRB-SC4 (core plate)	S235JR	0.15	38.21	257	363	1.41	195
BRB-SC5 (core plate)	S355JR	0.19	25.45	373	543	1.46	204
RT-S (outer tube)	S355JR	0.38	18.35	345	509	1.48	189

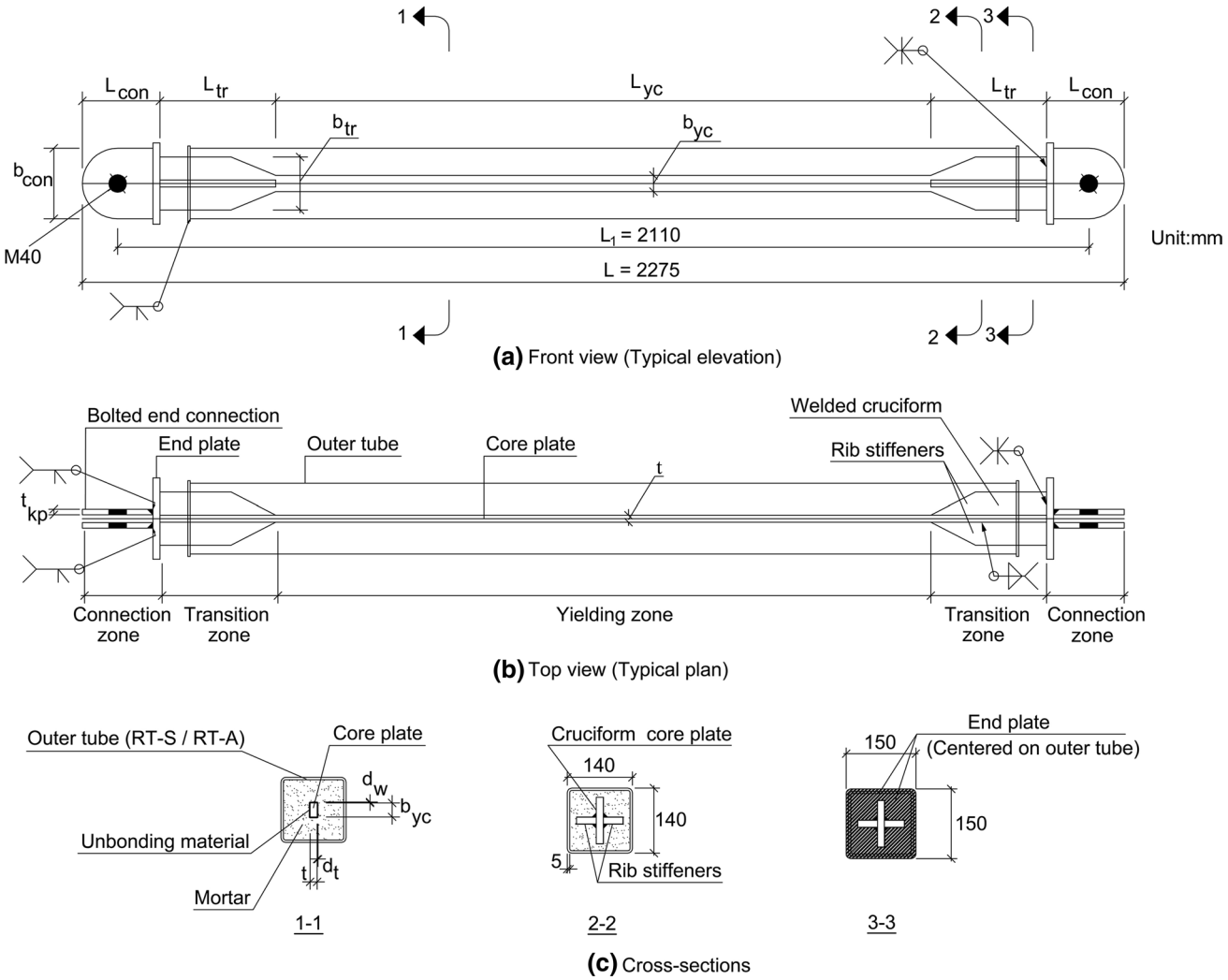

Fig. 2 Specimen configurations for bolted end connection BRBs

The cross-section of the cores is defined based on the setup capacity. Full-scale BRB specimens had rectangular steel plates (15 mm × 35 mm for BRB-AC1, 15 mm × 40 mm for BRB-AC3, 16 mm × 30 mm for BRB-SC4, and 12 mm × 25 mm for BRB-SC5), which expand at both ends to form a cruciform section. The cruciform sections in BRB-AC1, BRB-SC4 and BRB-SC5 are formed by fillet welded rib stiffeners on each side of the core. Additionally, complete joint penetration (CJP) groove welds were applied to connect the core and stiffeners to the end plate (Fig. 2a, b). For BRB-AC3, four aluminum alloy angle members are bolt-assembled around the core to prevent the weak axis buckling of the core in the unrestrained region and avoid the low-cycle fatigue performance degradation caused by the welding of rib stiffeners. The cross-section properties of the outer tubes were 140 mm × 140 mm × 5 mm and 150 mm × 150 mm × 4 mm for the steel and aluminum braces, respectively. The cross-section of the steel cores is reduced in their middle (so-called yielding zone) to ensure early yielding and thus provide efficient ductile behavior. The total length of the BRBs (L) was limited to a constant value of 2275 mm as a constraint of the available test set-up. The work-point to work-point length is 3339 mm. The pin-to-pin length of BRB-AC1, BRB-SC4 and BRB-SC5 (L_1) was limited to a constant value of 2110 mm. The ratio of the yielding core to the total length of the brace (L_{yc}/L) for common BRBs (except for short-core BRBs) normally varies from 0.6 to 0.8 according to Sabelli et al. (2003), Tremblay et al. (2006) and Tsai et al. (2004). For this reason, $(L_{yc}/L_1) \geq 0.6$ for BRB-AC1, BRB-SC4, BRB-SC5 and $(L_{yc}/L) > 0.6$ for BRB-AC3 were considered for the sizing of the braces (Table 3). Finally, the core yielding lengths were selected at approximately 67% of the total brace length ($L_{yc} \leq 1410$ mm). Core lengths of the BRBs are determined based on several design issues such as end connections, yield stress of the core material, cross-sectional dimensions of the

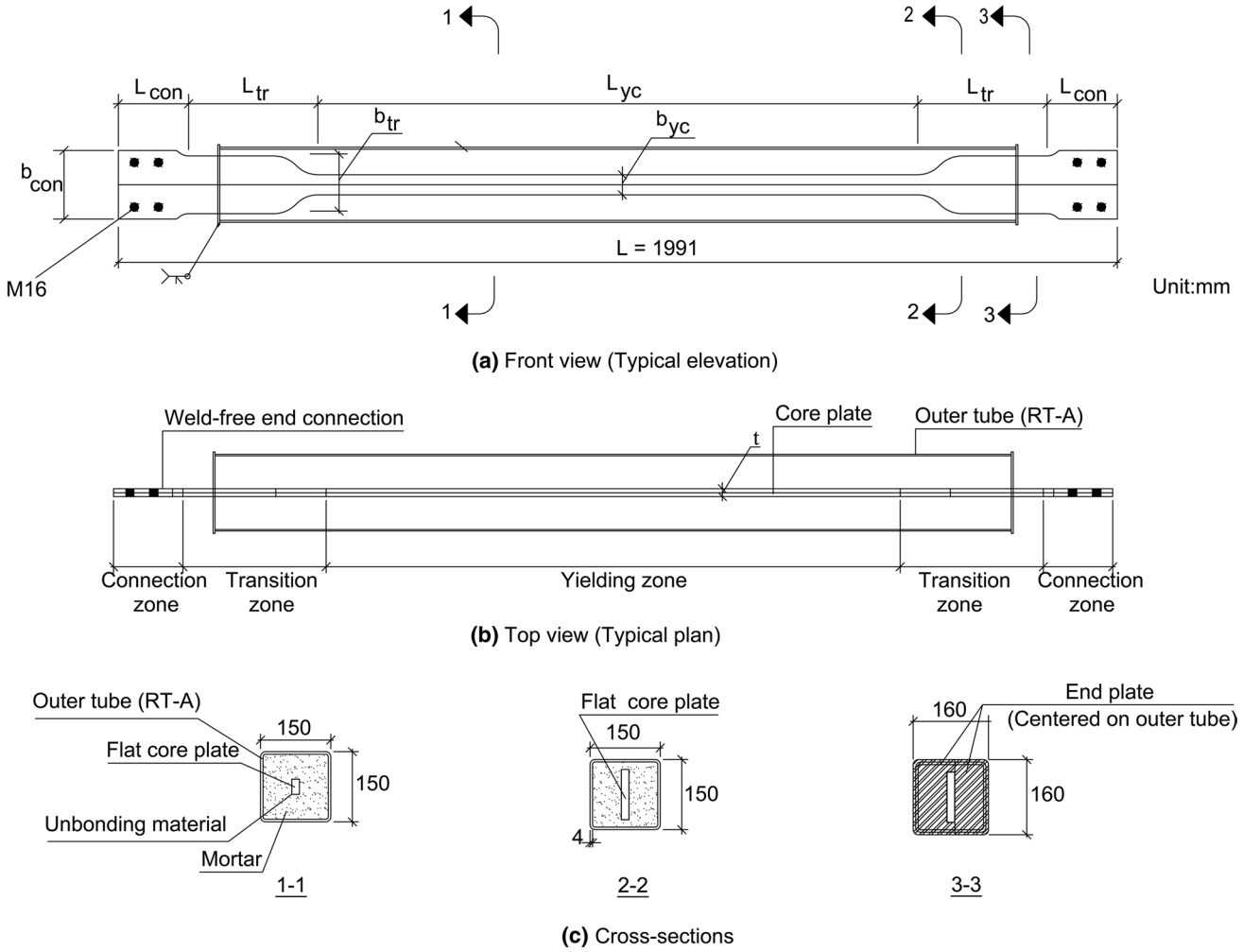

Fig. 3 Specimen configurations for weld-free end connection BRBs

Table 3 General geometrical parameters of the specimens

Specimen	L_{yc} (mm)	b_{yc} (mm)	t (mm)	L_{con} (mm)	b_{con} (mm)	L_{tr} (mm)	b_{tr} (mm)	L_{yc}/L
BRB-AC1	1278	35	15	184	165	315	115	0.61
BRB-AC3	1195	40	15	140	137	258	115	0.60
BRB-SC4	1410	30	16	185	165	249	100	0.67
BRB-SC5	1380	25	12	184	165	264	98	0.65

core material, and β (compression strength adjustment factor) and ω (strain-hardening adjustment factor) coefficients used (Avci-Karatas 2013). Therefore, special attention was paid on to have as close as possible yielding length (max. 10% difference) for the developed BRBs. Under similar conditions, it is clear that BRBs with longer yielding parts would dissipate more energy. However, this difference is small in this work. The ratio of the Euler buckling load, P_e/P_{yc}, of the outer tube (P_e) to the yield load of the core (P_{yc}) need to be checked as a criterion to ensure the yielding of the core material. Watanabe et al. (1988) suggested that this ratio should be larger than 1.5. Relatively higher ratios of 12.7 and 14.2 for BRB-AC1 and BRB-AC3 and 30.9 and 32.1 for BRB-SC4 and BRB-SC5 were used in this work, mainly due to the locally available tube cross-sections and to provide overall stability. The contributions of mortar and the core to the buckling resistance of the brace have been eliminated by the existence of the unbonded surface.

Special unbonding (or debonding) materials are adopted for the interface of the core and high strength mortar to reduce friction between core and restraining members (outer tube plus mortar). In the proposed BRBs, a three-layer interface has been

utilized: the core was first coated with polytetrafluoroethylene (Teflon) tape and then lubricated with rubber grease (for BRB-AC1, BRB-SC4, and BRB-SC5). Differently, BRB-AC3 also used air bubbles on top of the previously defined unbonded surface. The purpose of using air bubbles was to provide shear flexibility to guarantee an even sliding surface and to allow a more transversal expansion gap of the core when compressed. Although BRBs and other metallic devices are considered insensitive to temperature increase when the brace is subjected to large displacement reversals (Symans et al. 2008), these air bubbles may lose their properties near the fracture of the brace. Since air bubbles are only the top layer of the whole unbonded surface, this possible damage does not negatively affect the brace behavior.

As shown in the cross-sectional detail of BRBs in Fig. 2c (Cross-Sect. 1-1,), the unbonding material was selected to have a gap thickness of d_t (approximately 0.5–10% of the core plate thickness of t) in the plate thickness direction of the core and a gap thickness d_w (approximately 0.5–10% of the core plate width of b_{yc}) in the plate width direction (Takeuchi et al. 2000). Generally, gaps with a thickness of 1.5 mm (including the unbonding material thickness) were used to minimize friction between the core and mortar for each side.

According to the Seismic Provisions for Structural Steel Buildings (AISC 341-10 2010), the axial yield strength of core, P_{yc}, shall be determined as per Eq. (1):

$$P_{yc} = \beta\omega R_y F_{yc} A_c \tag{1}$$

where β and ω are, as stated above, compression strength adjustment factor and strain-hardening adjustment factor, respectively; R_y is the ratio of the expected yield stress to the specified minimum yield stress; F_{yc} is the specified actual yield stress of the core as determined from coupon tests; and A_c is the net area of the core. ω is calculated as the ratio of the maximum tension force (T_{max}) measured from the qualification tests to the yield force, P_{yc}, of the test specimen. The compression strength adjustment factor, β, is calculated as a ratio of the maximum compression force (P_{max}) to the maximum tension force of the tested specimen. AISC 341-10 puts a limit on β (i.e., $\beta < 1.3$) to ensure a relatively symmetrical hysteretic response. For preliminary design purposes and prior to tests, for the steel core BRBs, numerical values of β and ω at the point of the maximum displacement level were taken from previous studies (Merritt et al. 2003; Lopez and Sabelli 2004) as $\beta = 1.15$ and $\omega = 1.45$. Since previous studies focused on steel core BRBs, for the aluminum alloy core BRBs, β was also assumed to be 1.15. Since no significant data were available for ω values in aluminum alloy BRBs, the strain-hardening properties of coupon tests were used to predict ω values as 1.73 and 1.81 for BRB-AC1 and BRB-AC3, respectively. The factor R_y need not be applied if P_{yc} is established using yield stress determined from a coupon per the AISC 341-10.

4 Description of the Test Set-up, Instrumentation and Loading Protocol

A versatile test set-up that was previously designed and fabricated for the cyclic testing of regular braces was used in this work. The set-up was composed of a steel L-frame (a vertical steel I-shaped column hinged on top of the I-shaped steel foundation beam that was attached to a strong floor) was designed to accommodate different bracing types and lengths (Fig. 4) (Haydaroglu et al. 2011). The foundation beam was attached to the existing reinforced concrete strong floor using closely spaced threaded tiedown rods. The test set-up was designed to remain elastic under a maximum actuator force of 250 kN. The steel grade used for the test set-up was S275JR. A displacement-controlled loading protocol, proposed by AISC 341-10, was used for all BRB tests.

The instrumentation for the experiments was designed to measure the global response of the test set-up and the local performance of BRBs. The testing was carried out and monitored via linear variable displacement transducers (LVDTs) that were mounted on the column face at the same height as the actuator. Post-yield strain gauges (at locations of 1/4, 2/4, 3/4 points of the outer tube length and on each face as well as at the gussets) and several LVDTs were installed at critical points of the set-up. The LVDT and strain gauge layouts were identical for all specimens. The labels and locations for LVDTs and uniaxial strain gauges are shown in Fig. 5a. Several LVDTs were used to monitor the accidental movement of the frame with respect to the strong floor (e.g., at the mid-height of the column, on the gusset plates and the foundation beam). The applied load was measured by a load cell mounted on the actuator. In total, 17 strain gauges were used for each BRB test. In this experimental work, a unique strain gauge configuration to monitor the behavior of the yielding core is also suggested for the inside of the BRB cores. During BRB manufacturing, a strain gauge (labeled as BRBKN) was placed in the middle of the core surface with a special technique (Fig. 5b). Further details about this can be found in Avci-Karatas (2013). No strain gauges were attached to the beam and column since these were designed to remain elastic at the maximum applied actuator load in preliminary BRB tests.

Lateral loads were applied by a servo-controlled hydraulic actuator (mounted between the set-up and strong RC wall). The displacement (or stroke) capacity of the actuator was ± 300 mm. The data were collected via a data acquisition system. Quasi-static reversed cyclic testing in this subassemblage configuration was carried out for each BRB based on the acceptance criteria given in the AISC 341-10 loading protocol. The top lateral displacement is

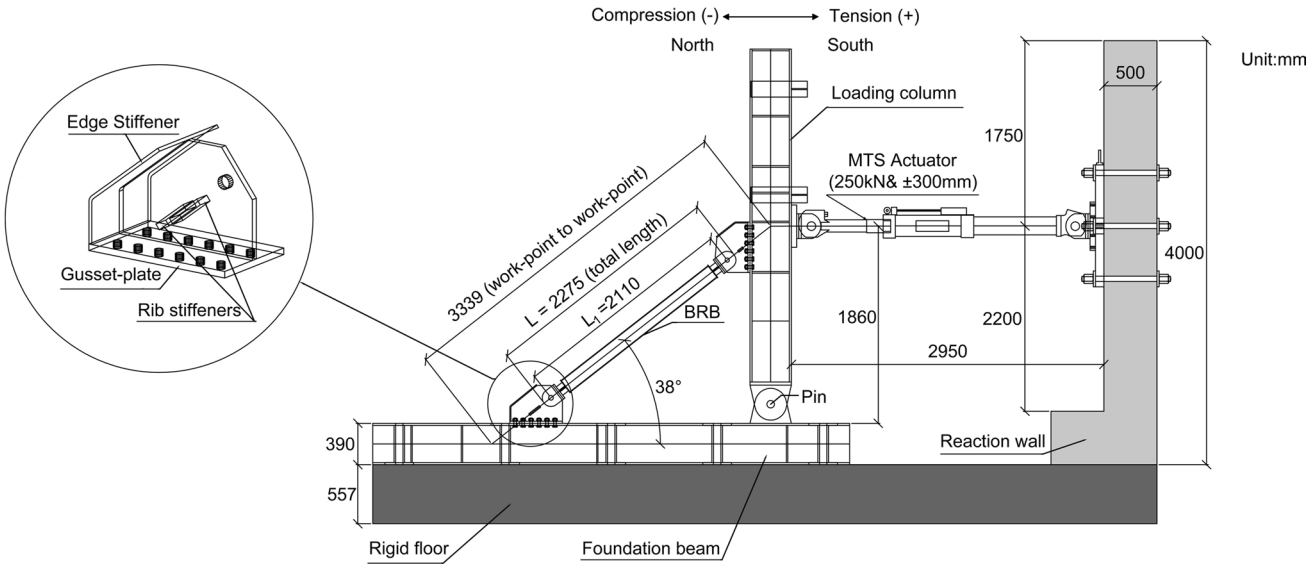

Fig. 4 Testing set-up with details of the gusset plate

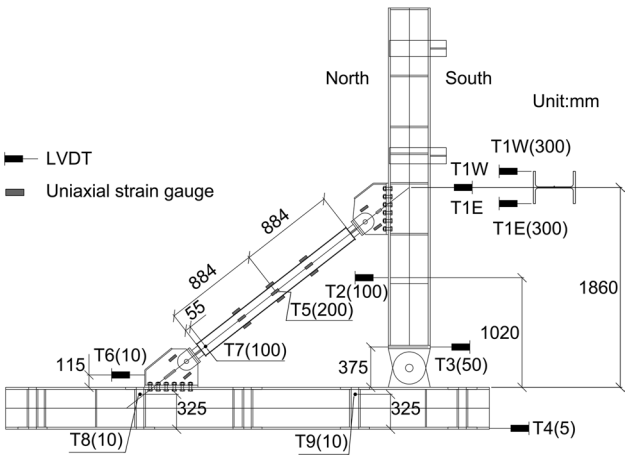

Fig. 5 Location of linear variable displacement transducers (LVDTs) and uniaxial strain gauges

related to the brace axial displacement and was taken as the displacement control parameter. The loading protocol used for the specimens is depicted in Fig. 6. Note that in the same figure, the vertical axis is set with the first axial yielding displacement of BRB, Δ_{by}. Here, Δ_{by} was calculated using the pin-to-pin distance (L_1) of the core plate in BRB-AC1, BRB-SC4, and BRB-SC5 based on previous research experience in the literature (Merritt et al. 2003; Vargas and Bruneau 2006). However, in BRB-AC3, the total length of the BRB is taken into consideration, as also assumed in (Vargas and Bruneau 2006). To establish the value of Δ_{by}, the inelastic displacement of the core plate in the yielding length was considered at the actual yield force level. Additionally, the elastic displacement of the core plate outside the yield length at each end of the core is included. The brace displacement at the design story drift, Δ_{bm}, was taken as $5\Delta_{by}$, as proposed by AISC 341-10. It was proposed that the design story drift not be calculated as less than 0.01 times the story height ($\Delta_{bm}/h > 0.01$). In the beginning, 2 cycles of the loading at each elastic displacement level of $1/4\Delta_{by}$, $2/4\Delta_{by}$, and $3/4\Delta_{by}$ were applied to the specimens. Figure 7 shows that all BRBs are installed in the test set-up and are ready for testing. Two gusset plates were placed at both ends to ensure proper anchoring to the test set-up. Specially designed gusset plates made of S355JR steel were used for the BRBs to avoid out-of-plane buckling (Fig. 4). To have mobility for the replacement of BRBs, gusset plates were designed as removable elements bolted to the test set-up. Rib and edge stiffeners were added to the gusset plates to improve the local and out-of-plane buckling capacity at the connection points.

5 Testing of BRB Specimens

The behavior of each specimen, both in the elastic and inelastic ranges, is reported herein. The system was loaded horizontally, developing axial tension and compression displacements in the diagonal braces. Note that positive (+) forces denote the loading case that generates tension in the brace, while the negative (−) forces denote the loading case that generates compression in the brace. The specimens were first subjected to a lateral load (towards the south) producing tension in the braces. The same conventions were adopted for all BRB tests. The percent drift

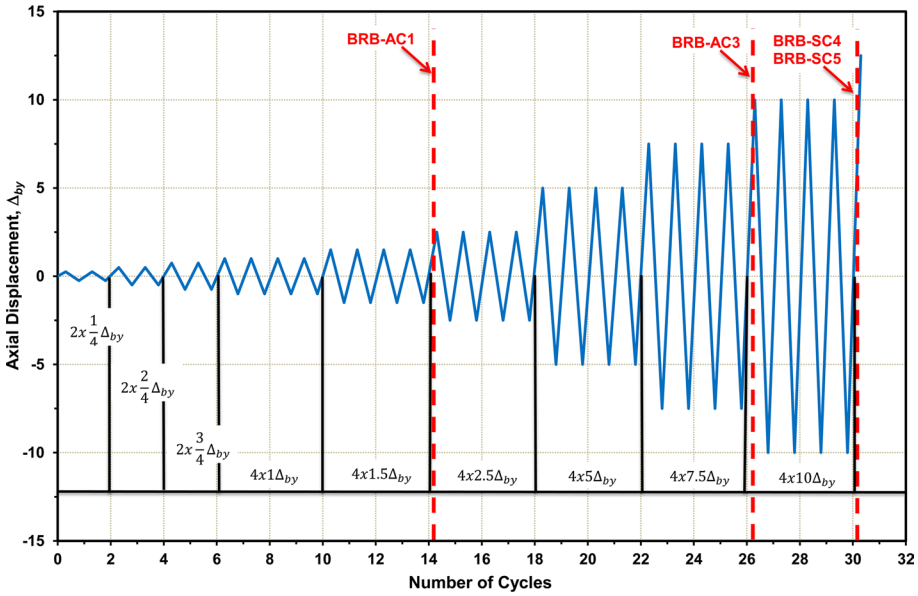

Fig. 6 Loading protocol

is computed as the ratio of lateral displacement divided by the vertical distance between the actuator axis and the top face of the steel foundation beam (1860 mm). Experimental lateral force-lateral displacement hysteretic curves representing the cyclic behavior and predicted pushover curves (both in tension and in compression) for BRB-AC1 and BRB-AC3 are given in Fig. 8a, b; for BRB-SC4, and BRB-SC5, they are given in Fig. 9a, b, respectively. On the other hand, additional effort has been made to include the axial load versus axial strain hysteretic curves to better evaluate the performances. The experimental axial force-axial strain curves of all specimens are shown in Fig. 8c, d for BRB-AC1 and BRB-AC3 and in Fig. 9c, d for BRB-SC4 and BRB-SC5, respectively. The axial force of the BRBs was geometrically calculated from the lateral force of the actuator by considering the angle of the loading column at each displacement step. The axial strain of BRBs was defined by the relative displacement divided by the original length of the yielding portion of the braces. Strain amplitude is the absolute value of the tension or compression strain of each cycle, while the total strain range $\Delta\varepsilon$ is the distance between them.

Images from the lower/upper end connections and openings/closings of the BRB end portions for the last cycles are depicted in Fig. 10a–d for BRB-AC1, BRB-AC3, BRB-SC4 and BRB-SC5, respectively. No deformations were observed in the bolt holes of the gusset plate for all BRB tests. The details of the loading sequence for inelastic cycles applied to the specimens and the experimentally obtained average peak values of Δ_{by}, ω, β, T_{max}, P_{max}, drifts, axial force, axial strain, strain ranges ($\Delta\varepsilon$) and number of failure cycles (N_f) are summarized and tabulated in Tables 4, 5, 6 and 7 for BRB-AC1, BRB-AC3, BRB-SC4, and BRB-SC5, respectively.

5.1 Specimen BRB-AC1

BRB-AC1 exhibited linear elastic behavior under the elastic displacement levels of $1/4\Delta_{by}$, $2/4\Delta_{by}$, $3/4\Delta_{by}$. The values of the BRBKN strain gauge (placed in the middle of the BRB yielding core) at the elastic displacements were obtained between 1100 and 1700 μ, both in tension and compression. BRB-AC1 reached its experimental yield displacement in the tension at 6.80 mm ($+1\Delta_{by}$, 0.37% drift) and + 81.24 kN for the lateral force. When the brace was in the compression, the lateral force value was measured to be − 99.67 kN. These specific values were determined based on the occurrence of a significant nonlinearity for the hysteretic curves, coupon test results, and especially the recordings obtained from the BRBKN strain gauge (approximately + 2300 μ). At the fourth and last tension excursion of $\pm 1\Delta_{by}$ (Cycle 10), BRBKN was damaged, and no data were gathered from this point on. The average values of T_{max}, P_{max}, ω, and β were reached while the displacement levels were + 88.56, − 104.32 kN, 1.00 and 1.18, respectively. When the specimen was subjected to $\pm 1.5\Delta_{by}$ (10.17 mm, 0.55% drift), the lateral force reached + 101.45 and − 123.21 kN. Some strength degradation was observed in the hysteretic curves during the fourth excursion at $+1.5\Delta_{by}$ due to the fracture initiation around the heat-affected zone (HAZ) in the ribs' welding areas. Note that the weld area and surrounding HAZ can change the metal (i.e., steel and aluminum alloy) properties in that area. For the stresses above the yield stress of the material, early cracks may form in the HAZ and this phenomenon may reduce ductility. The average values of T_{max}, P_{max}, ω, and β reached at this displacement level were + 108.51, − 122.37 kN, 1.23 and 1.13, respectively After these cycles, the core fractured

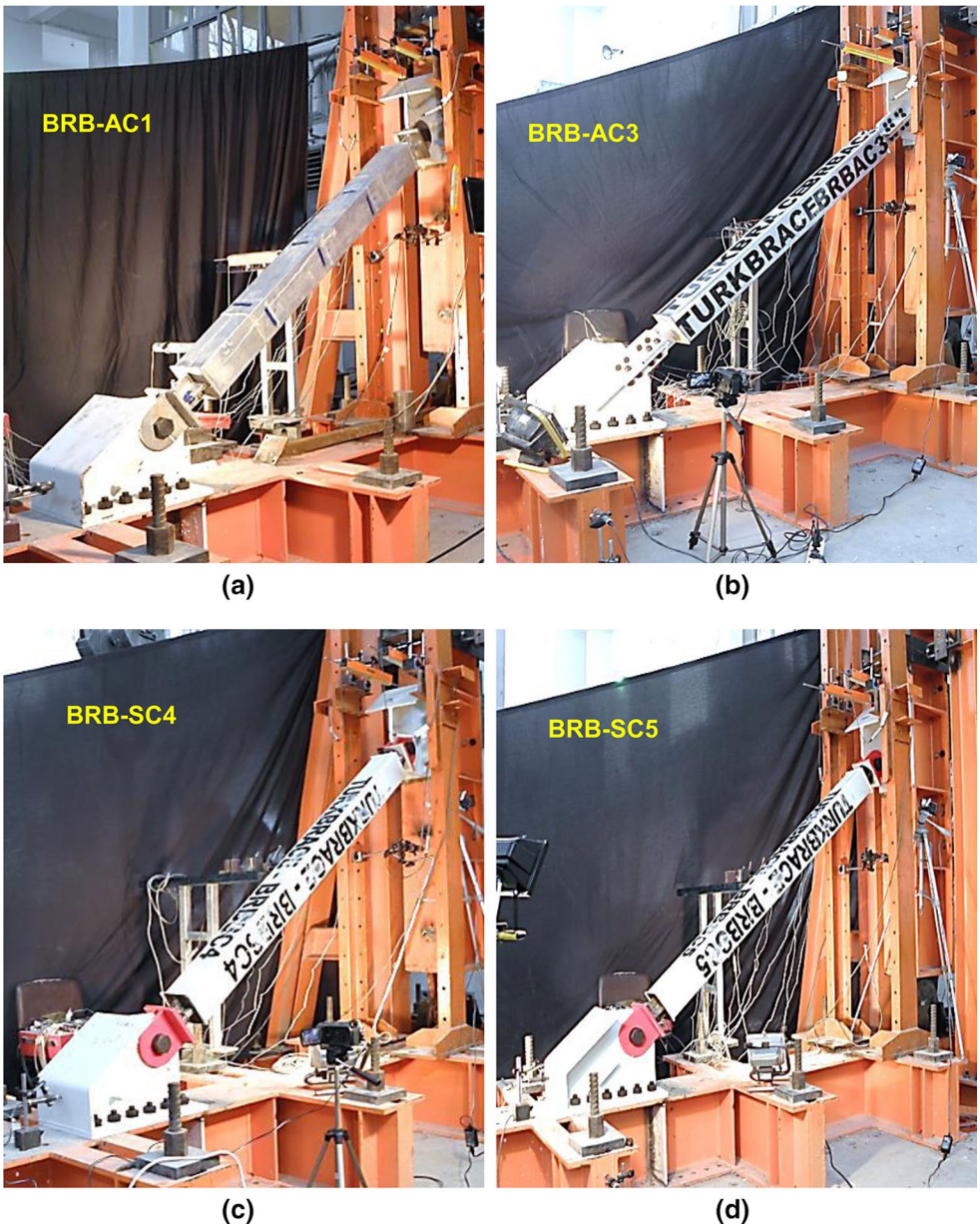

Fig. 7 Overall views from specimens prior to testing: **a** BRB-AC1; **b** BRB-AC3; **c** BRB-SC4; **d** BRB-SC5

at + 93.99 kN of lateral force and a lateral displacement of + 16.99 mm during the application of the first excursion of Cycle 15 ($\pm 2.5\Delta_{by}$, 0.91% drift). Due to the HAZ resulting from the detail design given in Fig. 2b in the transition zone, a premature failure in BRB-AC1 was experienced as the aluminum welds had an adverse effect on the failure mode. Out-of-plane displacements for the mid-span of BRB-AC1's outer tube (displacement measurement with LVDT-T5) were measured at between − 1.48 and + 1.24 mm. These values proved that out-of-plane buckling was effectively prevented during the test. Gusset plates and bolts performed well during the testing because the strain gauge recordings remained in the elastic ranges. Although BRB-AC1 was assumed to be a pilot test and behaved poorly when compared to other BRBs developed in this work, the testing of BRB-AC1 is of significance since the remainder of the BRB tests used the experiences gained from this testing.

5.2 Specimen BRB-AC3

BRB-AC3 exhibited linear elastic behavior under the first two cycles at 1.63 mm and 0.09% drift as well as during the two elastic cycles at 2/4 of the yield displacement (3.26 mm, 0.18% drift). In the elastic cycles, the lateral force values in

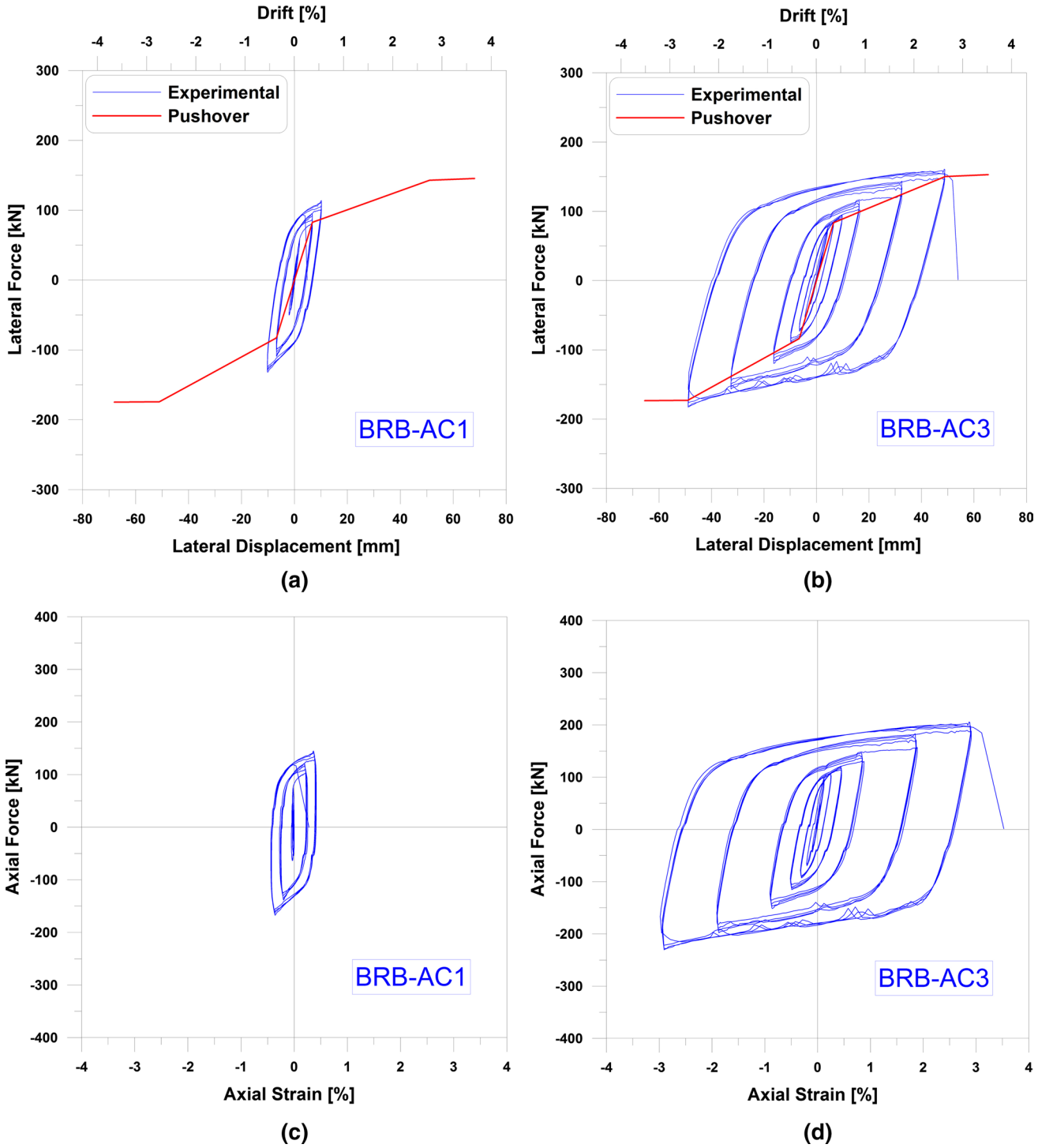

Fig. 8 Experimental hysteretic curves, predicted pushover curves, and force-strain relations of aluminum alloy BRBs: **a** BRB-AC1; **b** BRB-AC3; **c** BRB-AC1; **d** BRB-AC3

the compression loadings were less than those in the tension loadings. BRB-AC3 reached its experimental yield displacement in the tension at 6.52 mm ($+1\Delta_{by}$, 0.35% drift) and + 84.50 kN for the lateral force. When the brace is in compression, the lateral force reached − 71.25 kN. The values of BRBKN were + 2237 μ (brace in tension) and − 2242 μ (brace in compression) at the yielding cycles. The specimen was subjected to four cycles of $\pm 1.5\Delta_{by}$ (9.78 mm, 0.53% drift). The average lateral force obtained at this level was + 92.50 and − 87.50 kN. The BRBKN values

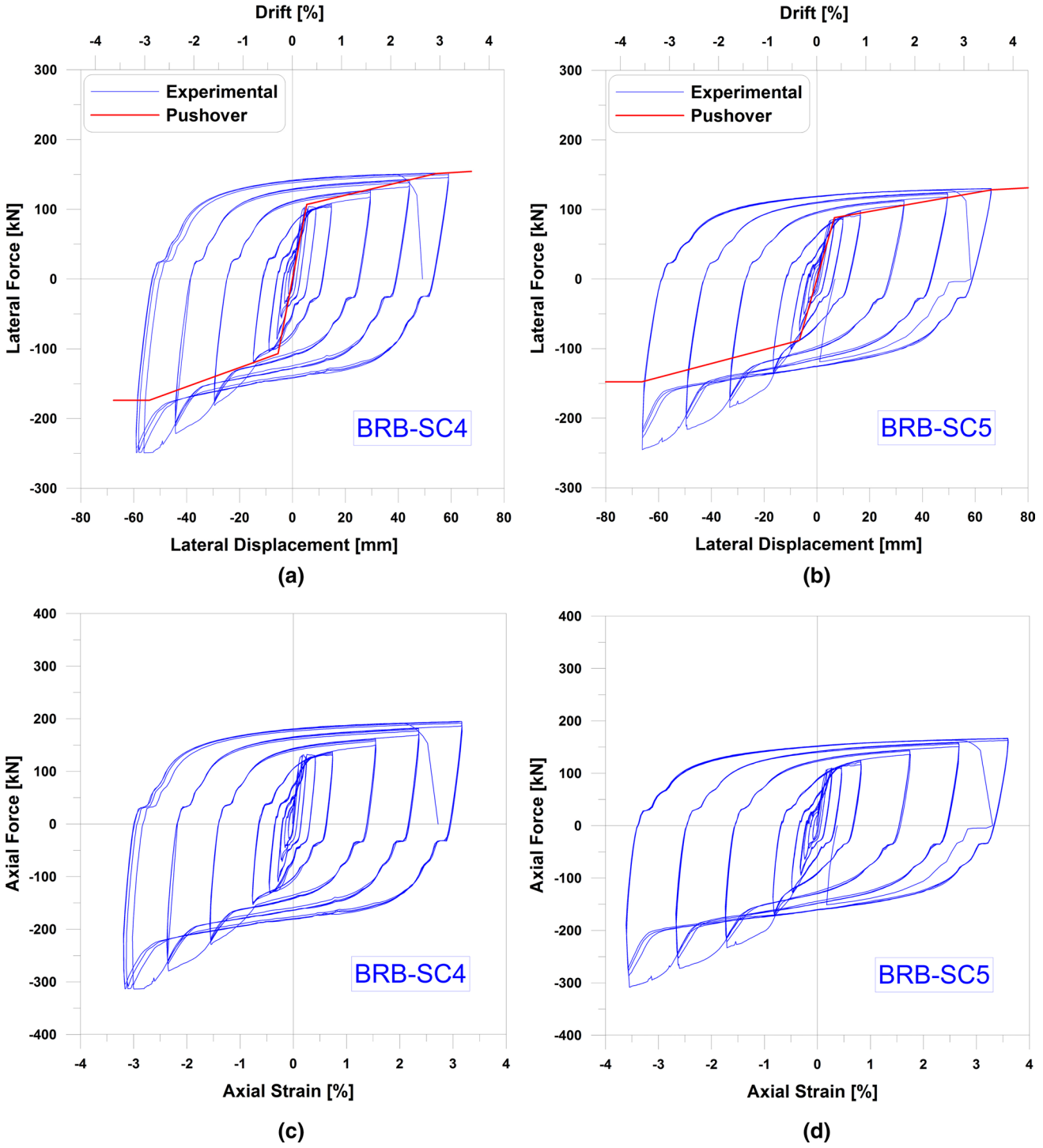

Fig. 9 Experimental hysteretic curves, predicted pushover curves, and force-strain relations of steel BRBs: **a** BRB-SC4; **b** BRB-SC5; **c** BRB-SC4; **d** BRB-SC5

were recorded as +3500, −3000 μ, and +3800, −2900 μ at the first and last cycles of $\pm 1.5\Delta_{by}$, respectively. During the 4th cycle at $\pm 2.5\Delta_{by}$ (16.30 mm, 0.88% drift) and $\pm 5\Delta_{by}$ (32.60 mm, 1.75% drift), no damage or strength degradation was recorded. Note that BRBKN was damaged at the level of $+2.5\Delta_{by}$ and that no data were available after this point. Some strength degradation was observed in the hysteretic curves during the last excursion at $+7.5\Delta_{by}$ (48.00 mm, 2.63% drift). The average lateral force obtained at this level was +153.25 kN in tension and −174.00 kN in

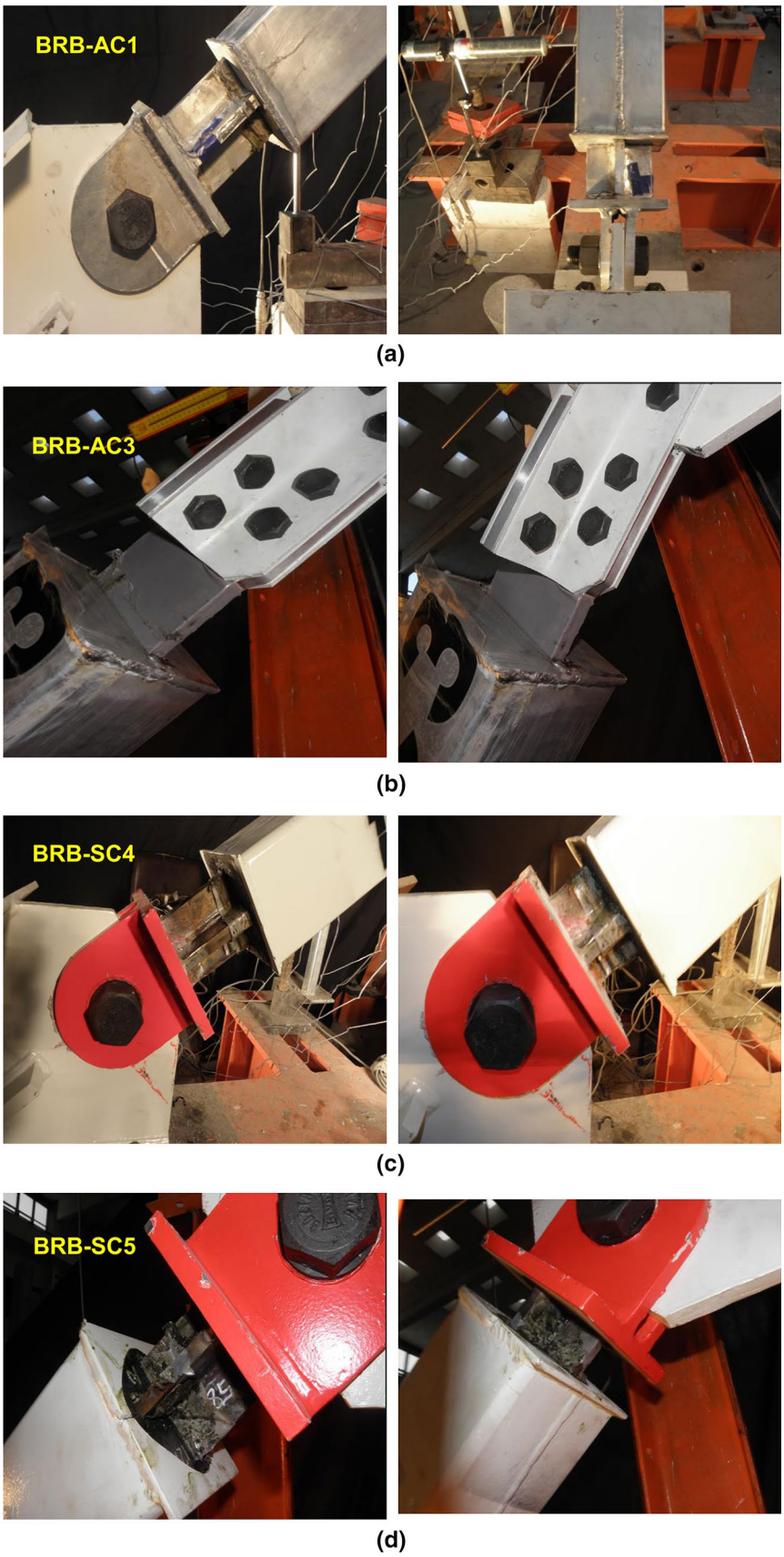

Fig. 10 Images from the upper and lower end connections, openings and closings of BRBs during the last excursions in tension and compression: **a** BRB-AC1 (lower end connection): $\pm 1.5\Delta_{by}$ ($10.17mm$, 0.55% drift); **b** BRB-AC3 (upper end connection): $\pm 7.5\Delta_{by}$ (48.90 mm, 2.63% drift); **(c)** BRB-SC4 (lower end connection): $\pm 10\Delta_{by}$ ($59.00mm$, 3.17% drift); **d** BRB-SC5 (upper end connection): $\pm 10\Delta_{by}$ (66.10 mm, 3.55% drift)

Table 4 Average peak response quantities and behavioral characteristics of BRB-AC1

BRB-AC1													
Cycle and axial displacement	Δ_{by} (mm)	T_{max} (kN)	P_{max} (kN)	β	ω	Drift (%)	Inelastic disp.	Axial force (kN)		Axial strain (%)		$\Delta\varepsilon$ (%)	N_f
								Tens.	Comp.	Tens.	Comp.		
$4x1.0\Delta_{by}$	±6.80	88.56	−104.32	1.18	1.00	0.37	–	112.30	−126.44	0.21	0.23	0.43	10
$4x1.5\Delta_{by}$	±10.17	108.51	−122.37	1.13	1.23	0.55	$4\Delta_{by}$	137.59	−158.35	0.38	0.38	0.76	14

Table 5 Average peak response quantities and behavioral characteristics of BRB-AC3

BRB-AC3													
Cycle and axial displacement	Δ_{by} (mm)	T_{max} (kN)	P_{max} (kN)	β	ω	Drift (%)	Inelastic Disp	Axial force (kN)		Axial strain (%)		$\Delta\varepsilon$ (%)	N_f
								Tens.	Comp.	Tens.	Comp.		
$41.0\Delta_{by}$	±6.52	84.50	−71.25	0.84	1.00	0.35	–	107.26	−90.22	0.25	0.31	0.56	10
$41.5\Delta_{by}$	±9.78	92.50	−87.50	0.95	1.09	0.53	$4\Delta_{by}$	117.50	−107.62	0.45	0.50	0.95	14
$42.5\Delta_{by}$	±16.30	108.75	−113.75	1.05	1.29	0.88	$12\Delta_{by}$	137.78	−143.06	0.85	0.88	1.73	18
$45\Delta_{by}$	±32.60	132.50	−149.25	1.13	1.57	1.75	$32\Delta_{by}$	169.75	−188.25	1.87	1.89	3.76	22
$47.5\Delta_{by}$	±48.90	153.25	−174.00	1.14	1.81	2.63	$52\Delta_{by}$	195.99	−219.14	2.90	2.92	5.82	26

Table 6 Average peak response quantities and behavioral characteristics of BRB-SC4

BRB-SC4													
Cycle and axial displacement	Δ_{by} (mm)	T_{max} (kN)	P_{max} (kN)	β	ω	Drift (%)	Inelastic disp.	Axial force (kN)		Axial strain (%)		$\Delta\varepsilon$ (%)	N_f
								Tens.	Comp.	Tens.	Comp.		
$41.0\Delta_{by}$	±5.90	102.00	−85.75	0.84	1.00	0.32	–	126.82	−106.31	0.25	0.29	0.54	10
$41.5\Delta_{by}$	±8.85	101.75	−102.75	1.01	1.00	0.48	$4\Delta_{by}$	127.89	−122.22	0.41	0.45	0.86	14
$42.5\Delta_{by}$	±14.75	104.50	−117.50	1.12	1.02	0.79	$12\Delta_{by}$	133.32	−142.53	0.74	0.77	1.51	18
$4x5\Delta_{by}$	±29.50	123.75	−172.00	1.39	1.21	1.59	$32\Delta_{by}$	155.54	−211.31	1.55	1.56	3.11	22
$47.5\Delta_{by}$	±44.25	138.25	−203.00	1.47	1.37	2.38	$52\Delta_{by}$	176.38	−251.59	2.36	2.37	4.73	26
$410\Delta_{by}$	±59.00	149.63	−247.38	1.65	1.47	3.17	$72\Delta_{by}$	191.44	−294.28	3.17	3.12	6.29	30

Table 7 Average peak response quantities and behavioral characteristics of BRB-SC5

BRB-SC5													
Cycle and axial displacement	Δ_{by} (mm)	T_{max} (kN)	P_{max} (kN)	β	ω	Drift (%)	Inelastic disp.	Axial force (kN)		Axial strain (%)		$\Delta\varepsilon$ (%)	N_f
								Tens.	Comp.	Tens.	Comp.		
$41.0\Delta_{by}$	±6.61	86.00	−73.13	0.86	1.00	0.36	–	107.77	−86.13	0.27	0.32	0.59	10
$41.5\Delta_{by}$	±9.92	87.13	−98.78	1.13	1.01	0.53	$4\Delta_{by}$	110.09	−125.05	0.46	0.48	0.94	14
$42.5\Delta_{by}$	±16.53	94.13	−130.75	1.39	1.09	0.89	$12\Delta_{by}$	119.53	−165.05	0.82	0.82	1.64	18
$4x5\Delta_{by}$	±33.05	109.88	−165.00	1.50	1.28	1.78	$32\Delta_{by}$	140.00	−216.84	1.75	1.73	3.48	22
$47.5\Delta_{by}$	±49.58	119.75	−189.00	1.58	1.39	2.67	$52\Delta_{by}$	153.42	−247.70	2.67	2.65	5.32	26
$410\Delta_{by}$	±66.10	127.50	−225.00	1.76	1.48	3.55	$72\Delta_{by}$	162.80	−281.78	3.60	3.57	7.17	30

compression. The aluminum alloy core fractured at the first tension excursion of Cycle 27 ($+10\Delta_{by}$, 65.20 mm, 3.51% drift) and the peak response quantity at the failure point was found to be + 144.45 kN. The out-of-plane displacements of the mid-span of BRB-AC3's outer tube were measured at between − 2.82 and + 0.44 mm, providing that the out-of-plane buckling was effectively prevented. This testing was deemed to be successful based on these observations.

5.3 Specimen BRB-SC4

The displacement loading history for the first steel core BRB started with 2 cycles of loading at each of the elastic displacement values, corresponding to $1/4\Delta_{by}$ (1.35 mm, 0.07% drift), $2/4\Delta_{by}$ (2.71 mm, 0.15% drift), and $3/4\Delta_{by}$ (4.08 mm, 0.22% drift). The BRBKN values at the elastic displacements corresponding to $1/4\Delta_{by}$, $2/4\Delta_{by}$, and $3/4\Delta_{by}$ were all lower than ± 1300 μ. Since the strain recordings rapidly exceeded the yield values, no data after this point were available from BRBKN. For this reason, the experimental yield displacement value was assumed to be the basis of the occurrence of a significant nonlinearity in the hysteretic curve and the coupon test result. At + 102.00 kN of lateral force, BRB-SC4 reached its experimental yield displacement in tension at 5.90 mm ($+1\Delta_{by}$, 0.32% drift). When the brace was in compression, the recorded lateral force was − 85.75 kN. The core's yielding length of BRB-SC4 is 1410 mm. Using these values, the lateral yielding displacement was computed as 5.41 mm. As a next step, the specimen was subjected to four cycles of $\pm 1.5\Delta_{by}$ (8.85 mm, 0.48% drift). The average lateral force obtained at this level was + 101.75 and − 102.75 kN. During the 4th cycle at $\pm 2.5\Delta_{by}$ (14.75 mm, 0.79% drift), $\pm 5\Delta_{by}$ (29.50 mm, 1.59% drift), and $\pm 7.5\Delta_{by}$ (44.25 mm, 2.38% drift), no damage or strength degradation was observed. Some strength degradation started to occur in the hysteretic curves during the fourth excursion at $+10\Delta_{by}$ (59.00 mm, 3.17% drift). The obtained average tension and compression capacities for the brace are + 149.63 and − 247.38 kN, respectively. The steel core fractured while reaching up to the first tension excursion of Cycle 31 ($+12.5\Delta_{by,}$ 4.00% drift), and the peak response quantities at this level were found to be a lateral force of + 120.12 kN and a lateral displacement of + 50.14 mm. Note that the specimen did not reach at 4.00% drift and failed by tension fracture at 3.17% drift level as stated in Table 6. The measured out-of-plane displacements of the mid-span of BRB-SC4's outer tube were found to be between − 1.64 and + 1.24 mm. Note that the out-of-plane buckling of the brace was effectively prevented during testing.

5.4 Specimen BRB-SC5

Two cycles for each elastic displacement level of $1/4\Delta_{by}$ (1.65 mm, 0.09% drift), $2/4\Delta_{by}$ (3.29 mm, 0.18% drift), and $3/4\Delta_{by}$ (4.94 mm, 0.27% drift) were taken into consideration. The BRBKN values were found to be + 1500 and − 740 μ for $1/4\Delta_{by}$, + 1588 and − 1000 μ for $2/4\Delta_{by}$, and + 1600 and − 1450 μ for $3/4\Delta_{by}$ displacement levels.

At + 86.00 kN of lateral force, BRB-SC5 reached its experimental yield displacement in tension at 6.61 mm ($+1\Delta_{by}$, 0.36% drift). When the brace was in compression, the lateral force value was measured as − 73.13 kN. While yielding occurred in the core, BRBKN was measured as + 1923 and − 1021 μ. These values were mostly the same yield strain levels obtained from the coupons. The brace core's yielding length of the specimen was 1380 mm. Using these values, the lateral yield displacement was calculated as 6.65 mm. This value was consistent with the experimental and static pushover results. At the end of Cycle 14 ($\pm 1.5\Delta_{by}$), stable hysteretic loops were found to be expected. The specimen was then subjected to four cycles of $\pm 1.5\Delta_{by}$ (9.92 mm, 0.53% drift). The average lateral force obtained at this level was + 87.13kN (brace in tension) and − 98.78 kN (brace in compression). At this level, BRBKN showed strain between 3500and3680 μ. The behavior of the brace was stable during the 4th cycle at $\pm 2.5\Delta_{by}$ (16.53 mm, 0.89% drift), $\pm 5\Delta_{by}$ (33.05 mm, 1.78% drift), $\pm 7.5\Delta_{by}$ (49.58 mm, 2.67% drift) and no damage was observed. Note that BRBKN was damaged at the first tension excursion of $2.5\Delta_{by}$ while the measurement was at $+3082\mu$.

Some strength degradation was recorded during the fourth excursion at $+10\Delta_{by}$ (66.00 mm, 3.55% drift). Experimentally obtained average tension and compression capacities for BRB-SC5 were + 127.50 and − 225.00 kN in tension and compression, respectively. The steel core fractured at the first tension excursion of Cycle 31 ($+12.5\Delta_{by}$, %4.44 drift) and the peak response quantities at this level were found to be a lateral force of + 112.53 kN and a lateral displacement of + 56.51 mm. The out-of-plane displacements of the mid-span of BRB-SC5's outer tube were measured at between ± 0.52 mm. Note that the out-of-plane buckling of brace was effectively prevented.

These steel core tests were also deemed to be successful tests, although some strength increases were found on the compression side. The possible reasons for this are discussed in the forthcoming sections.

6 Dissipated Energies, Cumulative Inelastic Displacements and Effective Damping Ratios

Using the experimental hystereses, some behavioral characteristics of the specimens, such as the maximum strength in tension and compression cycles, E_h cumulative hysteretic energy dissipations, η cumulative inelastic displacement (CID) values, and ξ_{effb} effective damping ratios are summarized and compared below (Avci-Karatas 2013; Celik et al. 2015).

For any cycle, the total area under the experimentally obtained hysteretic curve shows the dissipated energy through inelastic behavior. This is especially important in the evaluation of the seismic effectiveness of BRBs. The behavioral characteristics of the specimens are quantified with an emphasis on hysteretic energy dissipation. Since cumulative energy dissipation is a meaningful measure of the seismic efficiency of a structural system or component, the numerical values of the cumulative hysteretic energy E_h were calculated by a code developed using Matlab (Dindar 2009), and the variation of cumulative energy dissipation with the cumulative number of cycles is plotted in Fig. 11. As seen from this figure, the amount of dissipated energy at each cyclic loop increases with the increase in the lateral displacements. As expected, for elastic cycles, no energy dissipation was achieved by the specimens. Since the core shows similar behavior in tension and compression loadings, unlike a conventional buckling brace, the magnitude of the dissipated energy increases with the longer fracture life of the brace.

Table 8 η—cumulative inelastic displacement and E_h—hysteretic energy dissipation values

Specimen	η (CID)	E_h (kN mm)
BRB-AC1	$4\Delta_{by}$	14,852.70
BRB-AC3	$100\Delta_{by}$	137,301.40
BRB-SC4	$172\Delta_{by}$	248,507.90
BRB-SC5	$172\Delta_{by}$	244,763.50

The maximum values of the cumulative inelastic displacements (η) were obtained to be $4\Delta_{by}$ in BRB-AC1, $100\Delta_{by}$ in BRB-AC3 and greater than $172\Delta_{by}$ in both steel BRBs. These are for the last cycles' values that were reached during testing. Considering the entire cyclic patterns, the total CID values are calculated as $16\Delta_{by}$ and $672\Delta_{by}$ for BRB-AC1 and BRB-AC3 and $1360\Delta_{by}$ for steel BRBs, respectively. Note that AISC 341-10 requires the braces to achieve a cumulative inelastic axial displacement of at least $200\Delta_{by}$ before failure during BRB component testing. Achieving a CID of $200\Delta_{by}$ is a requirement for individual braces, but not for brace assemblages similar to the experimental testing method as followed in this study (Tsai et al. 2004). The numerical values of η and E_h that are reached by each specimen are summarized in Table 8.

The most common method for defining the effective damping ratio is to equate the energy dissipated in a cycle of the brace. The effective damping ratio (ξ_{effb}) can be obtained by the method proposed by Chopra (2001). In this method, the energy parameters represent any random cycle obtained

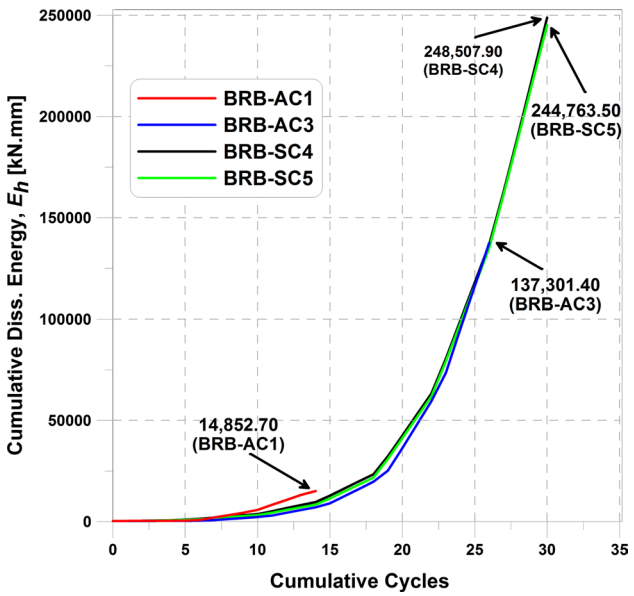

Fig. 11 Cumulative dissipated energy curves

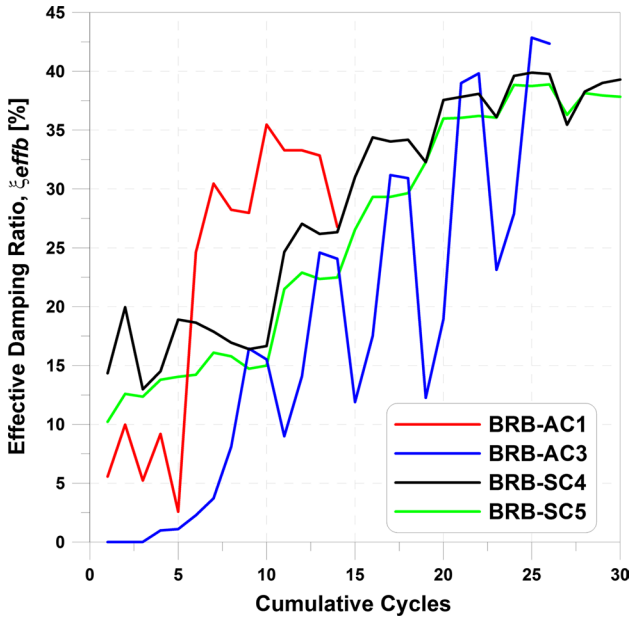

Fig. 12 Comparison of effective damping ratios

during the cyclic displacement reversals. Alternatively, as per EN 15,129 D.1 (2010) in 3.1.10, the effective damping of a seismic device that corresponds to dissipated energy during the cyclic response at the design displacement can be obtained by using Eq. (2). The force values cannot be considered equal when BRB is in tension ($T_{\Delta i}$) and compression ($P_{\Delta i}$). This expression is modified to take the difference of the design force values into consideration.

$$\xi_{effb} = \frac{E_{D,\Delta i}}{\pi \Delta_i \left(T_{\Delta i} + P_{\Delta i}\right)} \tag{2}$$

where $E_{D,\Delta i}$ is the dissipated energy per cycle. The experimental effective damping ratios at each cycle of BRB-AC1, BRB-AC3, BRB-SC4, and BRB-SC5 are compared in Fig. 12. The computed maximum values of ξ_{effb} were found to be between 27.97 and 35.47% for BRB-AC1, 8.10–42.85% for BRB-AC3, 16.40–39.89% for BRB-SC4, and 14.73–38.88% for BRB-SC5. Although these ratios had a tendency toward fluctuation at every cycle of testing, the damping ratios found had an increasing trend up to the maximum drift ratios reached. The maximum value of ξ_{effb} could be taken as a representative value of effective damping for any system. The maximum values were obtained at 0.37% and 0.55% drift ratios for BRB-AC1 and for BRB-AC3 and 2.38% and 2.67% drift ratios for BRB-SC4 and for BRB-SC5, respectively. Since ξ_{effb} is greater than 15% for BRB-AC3, BRB-SC4 and BRB-SC5, the tested BRBs can be classified as Energy Dissipating Devices (EDD) as per EN 15129 D.1.

7 Evaluation of Test Results and Comparisons of Observed Performance

The experimental hysteretic curves show full, stable, and repeatable behavior with no strength and stiffness degradation, even though the maximum strain amplitude was 3.60% in BRB-AC3's test. The stiffness values in the post yield region have slightly increased mainly due to the strain hardening effect. Up to the failure point (i.e., core fracture), no fracture in the welds, brace instability nor brace-to-gusset connection failures were observed in the BRBs. Note that the elastic tension parts of the hysteretic curves of the specimens were similar and close to the values obtained from the coupon test results. The force amplitude slightly decreases after the first cycles at each displacement step but tends to stabilize quite quickly.

The hardening properties of steel and aluminum materials have a significant impact on plastic strain distribution along the core plate. The experimental envelope curves (Fig. 13) obtained from Tables 5, 6 and 7 show that, for the same

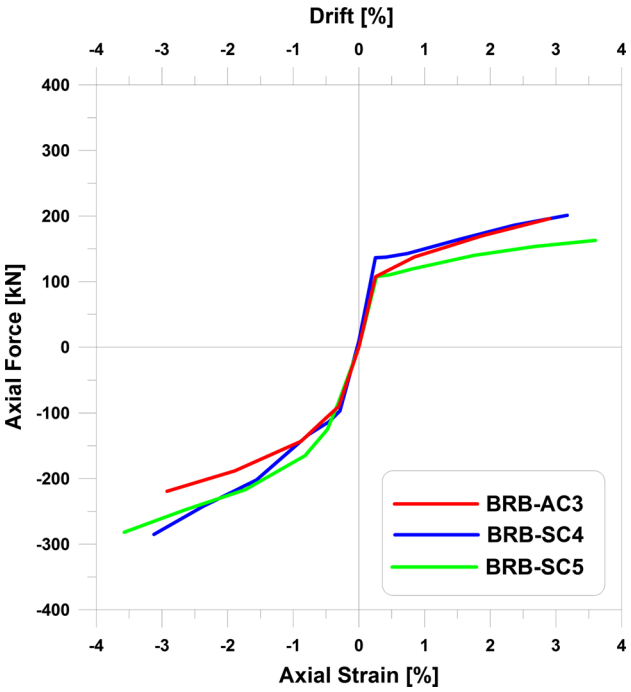

Fig. 13 Experimental backbones curves for BRB-AC3, BRB-SC4, and BRB-SC5

strength level on the compression side, the strain hardening ratios of the steel core BRBs are larger than the ratios obtained for the aluminum alloy specimens. It is observed that larger inelastic axial strains are obtained for aluminum alloy BRBs. However, on the tension side, BRB-SC5 has the minimum strain hardening properties, while BRB-SC4 and BRB-AC3 have similar behavior.

It is noteworthy to state that bolt slippage of the end bolts is effectively prevented in BRB-AC3 (with a weld-free end connection) leading to a smoother hysteretic loop. In addition, no deformation was observed near the bolt holes (i.e., no bolt slippage occurred). An unbonded surface with Teflon and air bubbles proved that a minimal force transfer can be achieved between the aluminum core and surrounding mortar, especially when covered with grease. Although the unbonded mechanism used in BRB-AC3 can successfully reduce the friction between the core and restraining members, the local sawtooth-like parts on the compression side of the hystereses at large compression cycles (Fig. 8b) are due to the irregular sequence of initiation and termination of local friction between the core and unbonded mechanism. Since the sawtooth-like parts of the hyteresis of BRB-AC3 are so local and since variations in compressive strength are quite less (max. 14.74%) this cannot produce any shocks in the structural components. However, in BRB-SC4 and BRB-SC5, the bolt slip effect is visible in the hystereses (Fig. 9a, b). According to AISC 341-10, depending on the means used to connect the test specimen to the subassemblage or test

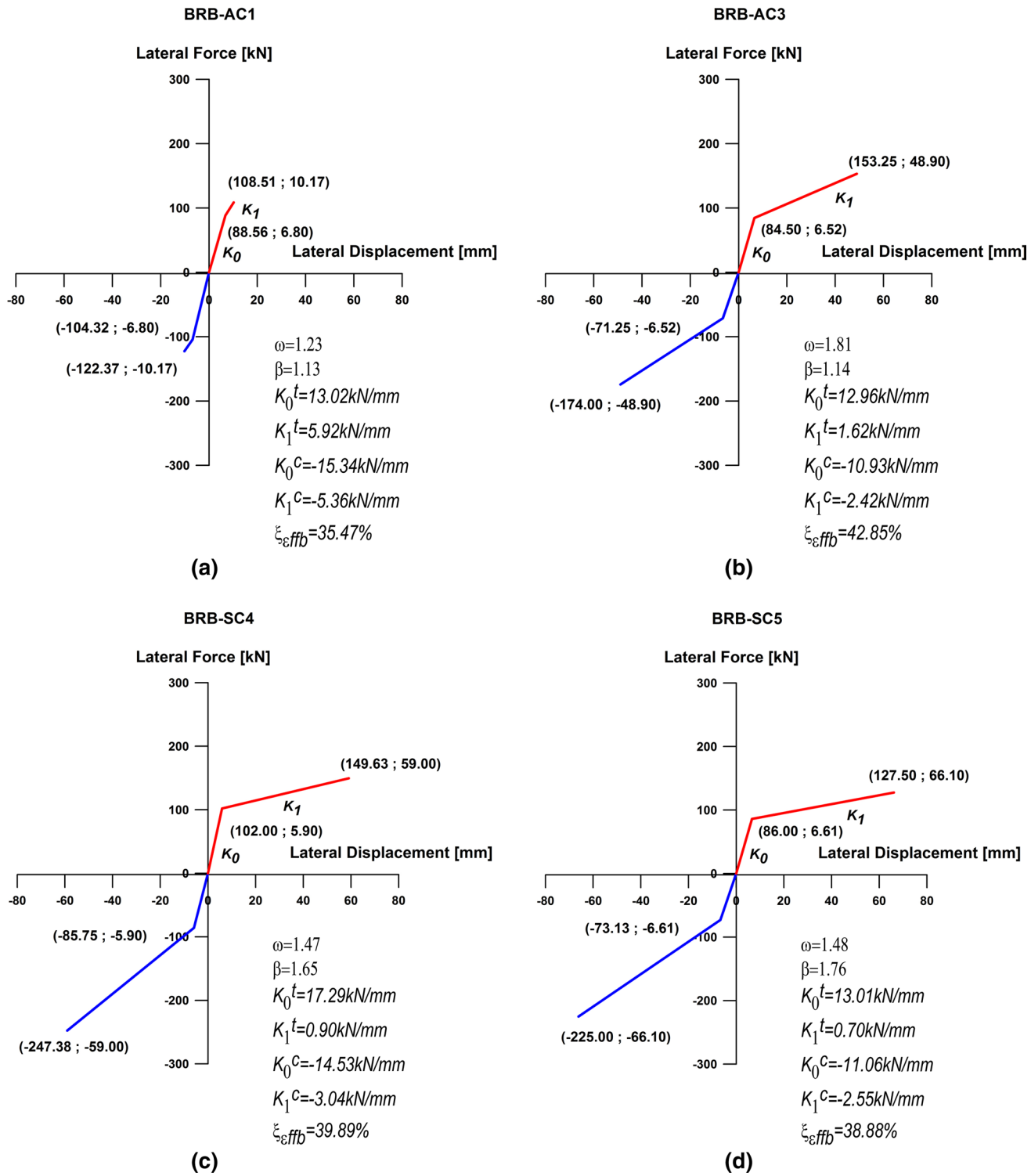

Fig. 14 Experimental bilinear force–displacement models: **a** BRB-AC1; **b** BRB-AC3; **c** BRB-SC4; **d** BRB-SC5

apparatus and the instrumentation system used, a bolt slip may appear in the load versus displacement history for some tests. This may appear as a series of downward spikes in the load versus displacement plot and is not generally a cause for concern provided that the behavior does not adversely affect the performance of the brace or brace connection. No negative effects of this type of slip were observed during the tests given in this study. Additionally, this has been observed in

other large-scale studies (e.g., Vargas and Bruneau 2006). As explained in Vargas and Bruneau (2006), the BRBs' behavior may not be significantly affected by the bolt hole size in a full-scale structure.

Bilinear experimental force–displacement relation models for the specimens and a numerical summary of the performance characteristics are determined and given in Fig. 14. Among the aluminum alloy BRBs, the highest strain-hardening adjustment factor at the maximum displacement level was found to be $\omega = 1.81$ in BRB-AC3. For all inelastic cycles, in both aluminum alloy specimens, the ratio of β factor did not exceed the allowable limit of $\beta = 1.3$ (AISC 341-10). The reached average tension and compression capacities for BRB-AC3 are + 153.25 kN and − 174.00 kN, respectively. For BRB-AC1, the reached average tension and compression capacities are + 108.51 kN and − 122.37kN, respectively. For inelastic cycles at $10\Delta_{by}$, the β factor exceeded 1.3 in both BRB-SC4 and BRB-SC5. At $10\Delta_{by}$, the average β factor values were found to be 1.65 (27% larger) for BRB-SC4 and 1.76 (35.4% larger) for BRB-SC5. The highest value of β was obtained in BRB-SC5. The compression side of the experimental hystereses of BRB-SC5 has higher values when compared to those obtained from the static pushover analysis. This overstrength in the compression side is attributed to a combination of a few reasons, as observed in other studies (Berman and Bruneau 2009; Merritt et al. 2003). For example, β was taken as 1.15 for predicting the pushover curves prior to testing. Note that the β coefficient covers every possible effect, including Poisson's effect. Poisson's ratio has numerical values of $0.3 \sim 0.5$ depending on the axial compression level in the brace. Therefore, the developed bilinear models given in Fig. 14 capture all above mentioned effects, including Poisson's effect in the compression side. Additionally, each specimen accommodates a sufficient number of gaps around the core plate to minimize Poisson's effect under large axial displacement amplitudes.

The inelastic tension excursions of steel BRBs are curved yet tend to become flat near the corner, revealing rather ductile behavior. This is also observed in the inelastic compression loading excursions, but their ends exhibit a sudden increase, leading to a sharper peak even in a reversal in the curvature of the excursion. This fact is common to most of the tested BRBs. This behavior is mainly due to the higher mortar contribution from friction forces generated by the steel core's multi-mode buckling (as evidenced from Fig. 17) with small longitudinal waves along the brace. However, this happens at larger drift values, especially when they are larger than 1.5%.

In addition, in the compression part of the BRB-SC4 and BRB-SC5, there are flat lines in the hysteretic curves, showing significant ductile behavior under cyclic loading. This behavior is characterized by weak isotropic hardening resulting in a bilinear force–displacement modeling, as shown in Fig. 14. The Baushinger effect is also observed in the hystereses.

The ratio of dissipated energies by the steel core BRBs (i.e., $E_{hBRB-SC4}/E_{hBRB-SC5}$) is found to be 1.02 while the same ratio for aluminum alloy BRBs (i.e., $E_{hBRB-AC3}/E_{hBRB-AC1}$) is found to be 9.24. Among all specimens, the highest hysteretic energy dissipation is achieved by BRB-SC4 mainly because the experimental fracture life of BRB-SC4 was longer than the other steel core BRB. The experimental fracture life of the steel BRBs was higher than the aluminum alloy core BRBs. Also, note that fatigue strength increases as the static tensile strength obtained from coupon tests increases (Campbell 2008). The aluminum alloys selected here are the types of locally available ones. As shown in Fig. 1, and Tables 1 and 2, lower ε_u values contributed to lower fracture life for aluminum alloy BRBs in this work.

Among the BRBs, the highest value of the effective damping ratio was obtained in BRB-AC3. The BRB-AC1 core plate fractured at the transition zone from the yielding section to the cruciform section (elastic part), mainly due to the presence of the HAZ. The occurrence of the plastic hinge at this affected point caused brace failure earlier than expected. For post-yield cycles for aluminum alloy BRBs, effective damping ratios fluctuate due to lesser (compared to steel BRBs) permanent deformations of aluminum alloy BRBs in reversed cyclic loadings (Fig. 12). This phenomenon is closely related to material science properties of aluminum alloy and steel. In brief, steel and aluminum alloy are called body-centered and face-centered cubic crystal structures, respectively (Beer et al. 2009). In addition to this, unsmooth loops in the compression cycles (resulted in changing β values) of the hystereses of BRB-AC3 would contribute to this zig-zag behavior of effective damping versus cumulative cycles curves. The ductility of steel is relatively higher than aluminum due to relatively low strain-rate sensitivity and Young's modulus, and this is further explained in (Bash and Shkaraputa 1988). For pre-yield cycles, effective damping ratios for steel BRBs are larger than the values obtained for aluminum alloy core BRBs. Generally speaking, the BRB made of normal yield strength steel core has a larger effective damping ratio when compared to the BRB made of high yield strength steel core.

Hysteretic curves showing out-of-plane displacements obtained from the specimens are shown in Fig. 15. These curves show that out-of-plane cyclic displacement histories are quite small, negligible and within the elastic/acceptable limits in the current experimental work. Also, as seen in the hysteretic curves given in Figs. 8 and 9, there is no significant drop in the compression strength which proves the fact that the braces did not buckle during testing. In case of elastically buckling braces, for example, out-of-plane

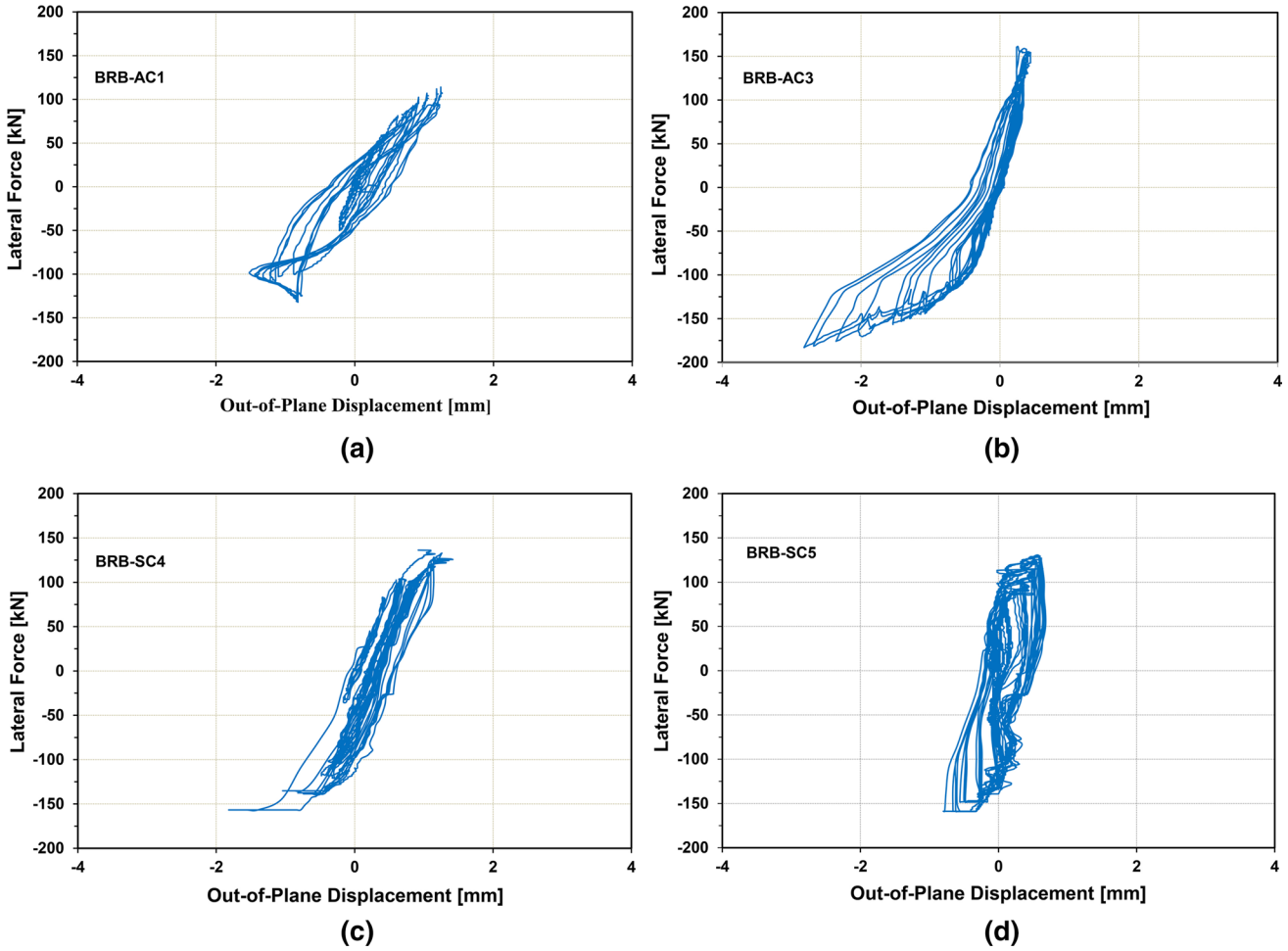

Fig. 15 Out-of-plane displacements hysteresis curves at mid span of BRBs; **a** BRB-AC1, **b** BRB-AC3; **c** BRB-SC4; **d** BRB-SC5

displacement values would reach up to (5 ~ 15)% of the clear brace length (e.g., Haydaroglu et al. 2011).

8 Low-Cycle Fatigue Life

The Manson–Coffin equation is often used to indicate the relationship between the number of failure cycles (N_f), and the total strain range ($\Delta\varepsilon$) can be found to be follows (Stephens et al. 2001):

$$\Delta\varepsilon = C_e\left(N_f\right)^{-k_e} + C_p\left(N_f\right)^{-k_p} \tag{3}$$

where C_i and k_i are constants that depend on the material. Because the inelastic strain of the core is much larger than its elastic strain, the total strain range can be directly taken into consideration. Equation (4) can be approximately written as follows:

$$\Delta\varepsilon = \overline{C}\left(N_f\right)^{-k} \tag{4}$$

Based on the test results conducted by Usami et al. (2012) for aluminum alloy BRBs, the obtained Manson-Coffin equations are expressed as follows:

$$\Delta\varepsilon = 0.056\left(N_f\right)^{-0.371} \text{ (for welded aluminum BRBs)} \tag{5}$$

$$\Delta\varepsilon = 0.070\left(N_f\right)^{-0.214} \text{ (for bolt-assembled, weld-free aluminum BRBs)} \tag{6}$$

Similarly, Usami et al. (2011) and Nakamura et al. (2000) proposed the following similar formulas for steel BRBs with welded end details, respectively:

$$\Delta\varepsilon = 0.210\left(N_f\right)^{-0.488} \tag{7}$$

$$\Delta\varepsilon = 0.204\left(N_f\right)^{-0.490} \tag{8}$$

As seen above, Eqs. (7) and (8) are almost identical and give very close results. Although the specimens tested in this

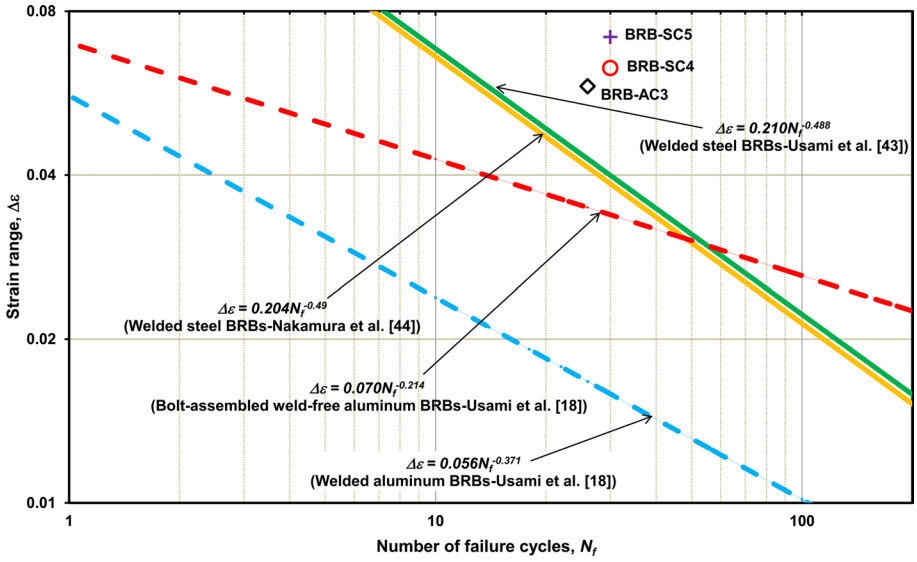

Fig. 16 Comparison of low-cycle fatigue curves

work do not exactly match the specimens tested by Usami et al. (2012, 2011) and Nakamura et al. (2000), it would be suitable to predict the low-cycle fatigue life by considering the previously proposed equations. For this reason, Fig. 16 is constructed, and based on this figure, the following observations can be made: Fig. 16 shows that the aluminum alloy core and steel-core specimens had a higher strain range ($\Delta\epsilon$) than predicted values by the proposed formulas. This reveals that the plastic deformation as well as energy dissipation capacities of the produced BRBs in this work is larger and promising. Despite the fact that Fig. 11 reveals that the cumulative dissipated energy values are much larger for BRB-SC4 and BRB-SC5 (compared to BRB-AC3), considering the low-cycle fatigue life as depicted in Fig. 16, which represents the number of failure cycles (N_f) and the total strain range ($\Delta\epsilon$), this difference is small. However, the performance of the steel core BRBs are, again, slightly better. This behavioral observation is attributed to the plastic strain distributions affected by the strain hardening properties of both materials used as the core members. It appears that BRBs with aluminum alloy cores have lower resistance to fatigue, as the maximum N_f is always lower in the case of aluminum (Tables 4, 5, 6 and 7).

9 Damage Patterns

Since most of the available BRB technologies do not allow for the inspection of damage after loading (or following an earthquake), a decision was made to cut the specimens in half to accurately detect the possible buckling forms and fracture zones. Figure 17 shows the buckled shapes and fracture zones of the cores.

BRB-AC1 fractured at the end of the transition zone (the end of welded rib stiffeners) due to the HAZ effect (Fig. 17a). The detailed fracture position and relationship of the HAZ is shown in Fig. 17e. Therefore, as discussed before, the performance of this brace was deemed to be poor. Satisfactory performance was observed in BRB-AC3: the core fractured nearly in the middle of the yielding zone because the peak stress occurring in this area was caused by the buckling modes in the core plate weak-axis direction. The multi-mode buckling of the core is visible in Fig. 17b, and the top view of the fractured spot is given in Fig. 17f. BRB-SC4 also exhibited a desirable mode of fracture. Again, the fracture zone is nearly in the middle of the yielding zone (midspan). The multi-mode buckled shape of the core is also given in Fig. 17c, and the side top view of the fractured spot is shown in Fig. 17g. In BRB-SC5, fractures occurred in approximately 65% of the yielding zone (midspan). Similar multi-mode buckled shapes were observed (Fig. 17d). The top view of the fractured spot is given in Fig. 17h. Note that since the number of buckling waves is high, the axial capacity of the braces was not negatively affected by this behavior. However, as discussed before, when the brace is subjected to compression forces, the lateral expansion of the steel core due to Poisson's effect and multi-mode buckling waves (since both of these produce contact forces) are other reasons for obtaining larger compression capacities and the corresponding β factors. No cracks or damage were apparent on the surface of the infill mortar. This would prove that the buckling prevention system (both mortar, steel/aluminum casing, and unbonded surface) that was developed in this study worked properly, especially up to the drift levels of 2%.

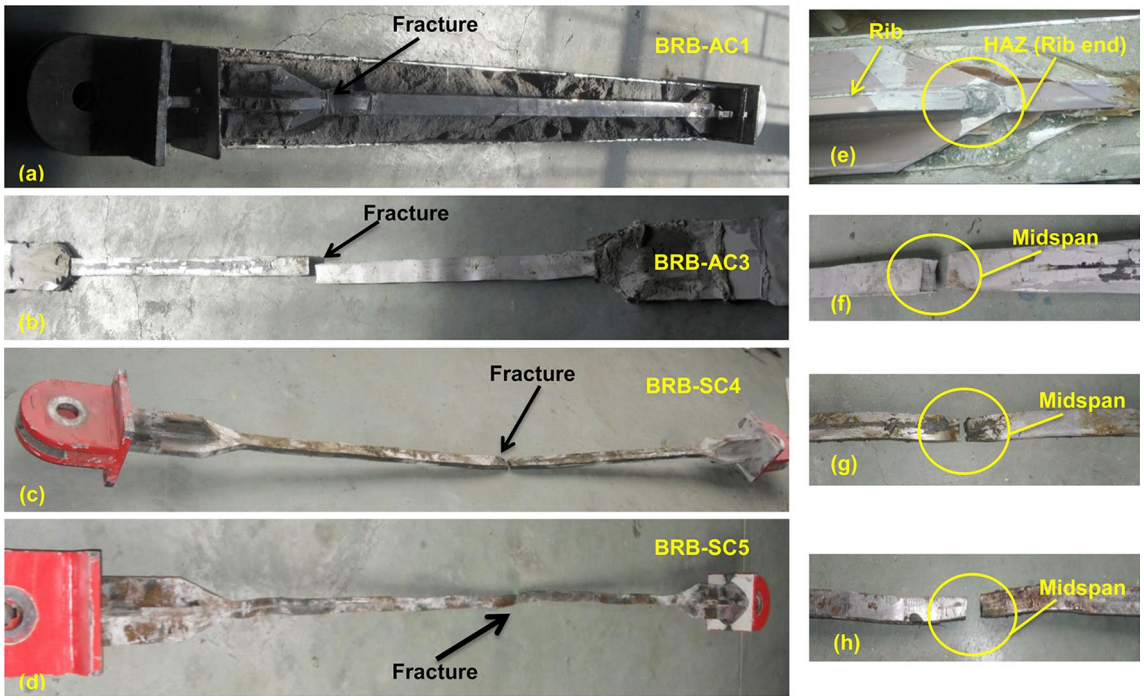

Fig. 17 Fractured zones of cores, visible residual plastic deformations, typical buckling waves, and failure positions; **a**, **e** BRB-AC1, **b**, **f** BRB-AC3; **c**, **g** BRB-SC4; **d**, **h** BRB-SC5

10 Conclusions

Four energy-dissipating aluminum alloy and steel core BRBs with the same yield strength and simple end details were tested under the cyclic displacement histories proposed by AISC 341-10. One major problem faced by licensed BRB manufacturers is potential corrosion problems that may shorten the expected life of braces and adversely affect their hysteretic behavior. To address this issue and to verify their effectiveness, two aluminum alloy core BRBs were designed, manufactured, and tested in addition to two steel core BRBs for comparison purposes. The findings from this experimental work could also provide significant information about the hysteretic characteristics of both types of BRB systems. All of the tests were performed until the braces fractured. The BRBs (except for BRB-AC1) showed satisfactory behavior with full hystereses. Hysteretic curves and behavioral values, such as the maximum strength in tension and compression cycles, effective damping ratios, and cumulative hysteretic energy dissipation values, are presented for each specimen. Based on the test results presented in this work, the following conclusions can be drawn:

1. BRB-AC1 with welded end connection details experienced a lower fracture life, mainly due to the HAZ. Other BRBs with weld-free (in BRB-AC3) and bolted (in BRB-SC4 and BRB-SC5) end connections performed well under the Standard Loading Protocol. No premature fracture, brace instability or brace end connection failures were observed.
2. Stable, repeatable hysteretic curves with positive incremental stiffnesses were obtained. Compared to steel core BRBs, aluminum alloy core BRBs showed relatively symmetrical hysteretic curves.
3. Considering the maximum value of $\beta < 1.3$, as proposed in AISC 341-10, the maximum experimental β factors at the maximum displacement values reached were found to be 1.13 (15% smaller) for BRB-AC1, 1.14 for BRB-AC3 (14% smaller), 1.65 (27% larger) for BRB-SC4 and 1.76 (35.4% larger) for BRB-SC5. Having higher β factors at larger drifts is attributed to the higher bond features of the mortar used, observed flaws/failures of the unbonding surface, and smaller amount of inner gap used.
4. The maximum effective damping ratios (ξ_{eff}) are found to be 39.89 and 38.88% for BRB-SC4 and BRB-SC5 and 35.47 and 42.85% for BRB-AC1 and BRB-AC3, respectively.
5. For the cases considered here, steel core BRBs dissipated larger hysteretic energy than the aluminum alloy core BRBs. The highest value for cumulative inelastic energy dissipation was obtained in BRB-SC4. For the steel core BRBs, BRB-SC4 demonstrated a slightly better ductile behavior than BRB-SC5 since this brace used

a normal yield strength steel core, resulting in greater dissipated energy and a better hysteretic response.

6. When bolted end connections are used for aluminum alloy BRBs, the fracture life significantly increased compared to the case of welded aluminum alloy BRBs. The use of weld-free aluminum alloy BRBs appears to be much more effective compared to other connection types. For this reason, weld-free aluminum alloy BRBs may be preferable in buildings or bridges in which severe corrosion effects are expected.

Acknowledgements This research was supported in part by the Scientific and Technological Research Council of Turkey (TUBITAK) for project number 110M776 and the Istanbul Technical University Research Projects Unit (ITU-BAP) for project number 33459. The steel core BRBs, gusset plates, and bolts used were donated by CIMTAS. The aluminum alloy outer tubes were provided by FENIS. The polytetrafluoroethylene bands of FIBERFLON were used as the unbonding surface. High strength mortar was donated by KOSTER. Technical assistance from the staff at Istanbul Technical University (ITU), the Structural & Earthquake Engineering Laboratory (STEEL) and Bogazici University's (BU) Civil Engineering Department and Structures Laboratory are gratefully acknowledged and appreciated. However, any opinions, findings, conclusions, and recommendations presented in this paper are those of the authors and do not necessarily reflect the views of the supporters and suppliers.

References

AISC. (2001). *Load and resistance factor design specification for structural steel buildings*. Chicago, IL: American Institute of Steel Construction.

AISC, SEAOC. (2001). *Recommended provisions for buckling-restrained braced frames*. USA: American Institute of Steel Construction/Structural Engineers Association of California.

ANSI, AISC 341–10. (2010). *Seismic provisions for structural steel buildings*. Chicago, IL: American Institute of Steel Construction.

ANSI, AISC 360–10. (2010). *Specification for structural steel buildings*. Chicago, IL: American Institute of Steel Construction.

ASTM A 370-08a. (2008). *Standard test methods and definitions for mechanical testing of steel products*. Philadelphia, PA: American Society for Testing and Materials.

ASTM E8, E8 M-09. (2009). *Standard test methods for tension testing of metallic material*. Philadelphia, PA: American Society for Testing and Materials.

Avci-Karatas, C. (2013). Design, fabrication, and cyclic behavior of steel and aluminum alloy core buckling restrained braces (BRBs). PhD dissertation, Istanbul Technical University (ITU), Istanbul, Turkey.

Bash, V. Y., & Shkaraputa, L. M. (1988). Stability with time of the strain hardening effect of constructional materials. *Strength of Materials, 20*(3), 358–362.

Beer, F. P., Johnston, E. R., Dewolf, J. T., & Mazurek, D. F. (2009). *Mechanics of materials* (6th ed.). New York: McGraw-Hill Companies.

Berman, J. W., & Bruneau, M. (2009). Cyclic testing of a buckling restrained braced frame with unconstrained gusset connections. *ASCE Journal of Structural Engineering, 135*(12), 1499–1510.

Campbell, F. C. (2008). *Elements of metallurgy and engineering alloys* (Vol. 1). Ohio: ASM International Book Co.

Celik, O. C., & Bruneau, M. (2009). Seismic behavior of bidirectional-resistant ductile end diaphragms with buckling restrained braces in straight steel bridges. *Engineering Structures, 31*(2), 380–393.

Celik, O. C., & Bruneau, M. (2011). Skewed slab-on-girder steel bridge superstructures with bidirectional-ductile end diaphragms. *ASCE Journal of Bridge Engineering, 16*(2), 207–218.

Celik, O. C., Yuksel, E., Avci-Karatas, C., Bal, A., Gokce, T., Bago, Z., et al. (2015). Component testing of steel-core buckling restrained braces (BRBs) with pinned end connections. In *Proceedings of the 8th ınternational conference advances in steel structures*, Lisbon, Portugal.

Chopra, A. K. (2001). *Dynamics of structures: Theory and Applications of earthquake engineering* (2nd ed.). Upper Saddle River, New Jersey: Prentice-Hall.

Chou, C. C., Chung, P. T., & Cheng, Y. T. (2015). Experimental evaluation of large-scale dual-core self-centering braces and sandwiched buckling-restrained braces. *Engineering Structures, 116,* 12–25.

Christopoulos, C., & Filiatrault, A. (2006). *Principles of passive supplemental damping and seismic isolation* (1st ed.). Pavia: IUSS Press.

CSI SAP 2000. (2009). *User's manual, version 14*. Berkeley: Computer and Structures Inc.

Di Sarno, L., & Elnashai, A. S. (2009). Bracing systems for seismic retrofitting of steel frames. *Journal of Constructional Steel Research, 65*(2), 452–465.

Di Sarno, L., & Manfredi, G. (2010). Seismic retrofitting with buckling restrained braces: Application to an existing non-ductile RC framed building. *Soil Dynamics and Earthquake Engineering, 30*(11), 1279–1297.

Di Sarno, L., & Manfredi, G. (2012). Experimental tests on full-scale RC unretrofitted frame and retrofitted with buckling-restrained braces. *Earthquake Engineering and Structural Dynamics, 41*(2), 315–333.

Dindar, A. A. (2009). Energy-based earthquake response analysis and design of reinforced concrete SDOF columns. Ph.D. dissertation, Bogazici University, Istanbul, Turkey.

EN 15129. (2010). *Anti-seismic devices*. European committee for standardization.

Fahnestock, L. A., Sause, R., Ricles, J. M., & Lu, L. W. (2003). Ductility demands on buckling-restrained braced frames under earthquake loading. *Earthquake Engineering and Engineering Vibration, 2*(2), 255–268.

FEMA 356. (2000). *Pre-standard and commentary for the seismic rehabilitation of buildings*. Washington, DC: Federal Emergency Management Agency.

Fujishita, K., Bal, A., Sutcu, F., Celik, O. C., Takeuchi, T., Matsui, R., & Terashima, M. (2015). Comparing hysteretic behavior of buckling restrained braces (BRBs) with bolted and welded end connections. In *Proceedings of the 8th ınternational symposium on steel structures (ISSS)*, Jeju, Korea.

Haydaroglu, C., Taskin, K., & Celik, O. C. (2011). Ductility enhancement of round HSS braces using CFRP sheet wraps. In *Proceedings of the 6th European conference on steel and composite structures (Eurosteel)*, Budapest, Hungary.

Kissell, J. R., & Ferry, R. L. (2002). *Aluminum Structures-A guide to their specifications and design* (2nd ed.). New York: Willey.

Lopez, W. A., & Sabelli, R. (2004). Seismic design of buckling-restrained braced frames. In *Steel tips*, Structural Steel Educational Council, Moraga, CA, USA.

Merritt, S., Uang, C. M., & Benzoni, G. (2003). Subassemblage testing of star seismic buckling-restrained braces. In *Rep. TR-2003/04*, Dept. of Structural Engineering, Univ. of California, La Jolla, CA, USA.

Nakamura, H., Maeda, Y., Sasaki, T., Wada, A., Takeuchi, T., Nakata, Y., et. al. (2000). Fatigue properties of practical-scale

unbonded braces. In *Nippon Steel Technical Report, 82, July* (pp. 51–57).

Pandikkadavath, M. S., & Sahoo, D. R. (2016). Analytical investigation on cyclic response of buckling-restrained braces with short yielding core segments. *International Journal of Steel Struct, 16*(4), 1273–1285.

Sabelli, R., Mahin, S., & Chang, C. (2003). Seismic demands on steel braced frame buildings with buckling-restrained braces. *Engineering Structures, 25*(5), 655–666.

Sahoo, D. R., Singhal, T., Taraithia, S. S., & Saini, A. (2015). Cyclic behavior of shear-and-flexural yielding metallic dampers. *Journal of Constructional Steel Research, 114,* 247–257.

Stephens, R. I., Ali, F., Stephens, R. R., & Fuchs, H. O. (2001). *Metal fatigue in engineering* (2nd ed.). New York: Willey.

Sutcu, F., Takeuchi, T., & Matsui, R. (2014). Seismic retrofit design method for RC buildings using buckling-restrained braces and steel frames. *Journal of Constructional Steel Research, 101*(10), 304–313.

Symans, M. D., Charney, F. A., Whittaker, A. S., Constantinou, M. C., Kircher, C. A., Johnson, M. W., et al. (2008). Energy dissipation systems for seismic applications: Current practice and recent developments. *Journal of Structural Engineering, 134*(1), 3–21.

Takeuchi, T., Hajjar, J. F., Matsui, R., Nishimoto, K., & Aiken, I. D. (2012). Effect of local buckling core plate restraint in buckling-restrained braces. *Engineering Structures, 44*(11), 304–311.

Takeuchi, T., Ida, M., Yamada, S., & Suzuki, K. (2008). Estimation of cumulative deformation capacity of buckling-restrained braces. *ASCE Journal of Structural Engineering, 134*(5), 822–831.

Takeuchi, T., Nakamura, H., Kimura, I., Hasegawa, H., Saeki, E., & Watanabe, A. (2000). *Buckling restrained braces and damping steel structures*. U.S. Patent 6 826 874, Dec. 12.

Takeuchi, T., Ozaki, H., Matsui, R., & Sutcu, F. (2014). Out-of-plane stability of buckling-restrained braces including moment transfer capacity. *Earthquake Engineering and Structural Dynamics, 43*(6), 851–869.

Tremblay, R., Bolduc, P., Neville, R., & DeVall, R. (2006). Seismic testing and performance of buckling-restrained bracing systems. *Canadian Journal of Civil Engineering, 33*(2), 183–198.

Tsai, K. C., Lai, J. W., Hwang, Y. C., Lin, S. L., & Weng, C. H. (2004). Research and applications of double-cored buckling restrained braces. In *Proceedings of the 13th world conference on earthquake engineering*, Vancouver, BC, Canada.

Usami, T., Ge, H. B., & Kasai, A. (2008). Overall buckling prevention condition of buckling-restrained braces as a structural control damper. In *Proceedings of the 14th world conference on earthquake engineering*, Beijing, China.

Usami, T., Ge, H., & Luo, X. Q. (2009). Experimental and analytical study on high-performance buckling-restrained brace dampers for bridge engineering. In *Proceedings of the 3rd ınternational conference on AESE*, San Francisco, California, USA.

Usami, T., Wang, C. L., & Funayama, J. (2011). Low-cycle fatigue tests of a type of buckling restrained braces. In *Proceedings of the 12th East Asia-Pacific conference on structural engineering and construction,* Hong Kong, China.

Usami, T., Wang, C. L., & Funayama, J. (2012). Developing high-performance aluminum alloy buckling-restrained braces based on series of low-cycle fatigue tests. *Earthquake Engineering and Structural Dynamics, 41*(4), 643–661.

Vargas, R. E., & Bruneau, M. (2006). Experimental investigation of the structural fuse concept. *Rep. MCEER-06-0005*, Multidisciplinary Center for Earthquake Engineering Research, Buffalo, NY, USA.

Vargas, R., & Bruneau, M. (2009a). Experimental response of buildings designed with metallic structural fuses. *ASCE Journal of Structural Engineering, 135*(4), 394–403.

Vargas, R., & Bruneau, M. (2009b). Analytical response and design of buildings with metallic structural fuses. *ASCE Journal of Structural Engineering, 135*(4), 386–393.

Wang, C. L., Usami, T., Funayama, J., & Imase, F. (2013). Low-cycle fatigue testing of extruded aluminium alloy buckling-restrained braces. *Engineering Structures, 46*(1), 294–301.

Watanabe, A., Hitomi, Y., Yaeki, E., Wada, A., & Fujimoto, M. (1988). Properties of brace encased in buckling-restraining concrete and steel tube. In *Proceedings of the 9th world conference on earthquake engineering*, Tokyo-Kyoto, Japan, pp. 719–724.

Zhao, J., Wu, B., & Ou, J. (2012). Effect of brace end rotation on the global buckling behavior of pin-connected buckling-restrained braces with end collars. *Engineering Structures, 40*(7), 240–253.